IEEE Access
Multidisciplinary | Rapid Review | Open Access Journal

Received August 1, 2020, accepted August 6, 2020, date of publication August 11, 2020, date of current version August 24, 2020.

Digital Object Identifier 10.1109/ACCESS.2020.3015722

Numerical Simulation and Analysis of Multicomponent Induction Logging Response in Anisotropic Formation

YUEHUI LI[1], XIANGYANG SUN[2], GUODONG SU[3], MIN WANG[1], AND RUI LI[1]

[1]School of Computer and Software Engineering, Xihua University, Chengdu 610039, China
[2]School of Electronic Science and Engineering (National Exemplary School of Microelectronics), University of Electronic Science and Technology of China, Chengdu 610054, China
[3]School of Electronic and Information Engineering, Fujian Polytechnic Normal University (Fuqing Branch of Fujian Normal University), Fuzhou 350300, China

Corresponding authors: Guodong Su (dongs0206@163.com) and Xiangyang Sun (63771514@qq.com)

This work was supported in part by the National Science Foundation of China under Grant 61727803; in part by the State's Key Project of Research and Development Plan under Grant 2016YFC0303502; in part by the Science and Technology Department of Sichuan Province under Grant 2017HH0083 and Grant 2017RZ0009; in part by the Ministry of Education of the People's Republic of China under Grant Z2012030; in part by the Xihua University under Grant Z1222624; and in part by the Yibin Kuntuoshen Electronic Technology Company Ltd.

ABSTRACT In this article, the response characteristics of multicomponent induction logging (MCIL) tool in anisotropic formation are analyzed. To solve the 1-D MCIL problems, we use a planar layered anisotropic medium (PLAM) Green's function (PLAMGF) method which is derived from the layered-medium Green's function (LMGF) and combined with MCIL excitation source and anisotropic formation environment, and then use it to investigate the equivalence of the MCIL tool responses in two models, i.e. the microscopic thin interbed formation and macroscopic anisotropic formation, and also analyze the effects of shoulder bed and formation dip on MCIL tools. In addition, in order to solve the complex 3-D problems, such as the effects of borehole, tool eccentricity and invasion on the tool response, we use the finite element method (FEM) based on a proposed new meshing scheme to simulate and analyze. This new meshing scheme includes two aspects: the use of cylindrical hexahedron element and the flexible meshing strategy combined with domain decomposition. Finally, some key detection performances of coaxial coils and coplanar coils of MCIL tool are studied. Numerical experiments are conducted to prove the effectiveness of our proposed method and provide the detailed results of the aforementioned aspects.

INDEX TERMS Multicomponent induction logging (MCIL), Green's function (GF), electric anisotropy, finite element method (FEM).

I. INTRODUCTION

Induction logging (IL) is an essential approach in the petroleum industry. It can provide electromagnetic (EM) and geometry information about the formation, thus playing an important role in evaluating hydrocarbon reservoir. A typical IL tool consists of one (or multiple) transmitting coil(s) to generate EM fields by applying an alternating current and one (or multiple) receiving coil(s) to measure the EM signals of the target. Thus, the formation resistivity (or conductivity) around the borehole can be obtained [1]–[3]. The thin sand-shale interbed formation is an important hydrocarbon reservoir, it usually exhibits macroscopic electrical anisotropy, and the vertical resistivity is usually much higher than the horizontal resistivity. However, the conventional IL tools can only measure the horizontal resistivity since they only have coaxial transmitter-receiver coils. This often makes the oil and gas reservoir overlooked or mistaken as water-bearing sand. In order to measure both the horizontal and vertical formation resistivity, the MCIL tool (or triaxial induction tool) has been developed [4]–[6]. As can be seen in Fig. 1, The MCIL tool is composed of three pairs of mutually orthogonal transmitter-receiver coils. Where, the coaxial coil pair means that the normal axes of the transmitting coil (T_z) and the receiving coil (R_z) are in the same direction (z-direction), and the coplanar coil pair

The associate editor coordinating the review of this manuscript and approving it for publication was Wei E. I. Sha.

means that the transmitting coil (T_x or T_y) and receiving coil (R_x or R_y) are in the same plane. As such the MCIL can measure the full matrix of nine magnetic components of the magnetic field. There are many researches on traditional array induction logging (AIL) [68]–[70], but few on MCIL, this is because this new tool has not only the traditional coaxial coil, but also the orthogonal coplanar coil, which makes the tool response more complex, so the analysis of MCIL problems still under developed. In recent decades, numerical simulation on MCIL tool responses has been extensively studied, which can be classified into three categories: the analytical methods [7]–[16], semi-analytical methods [17]–[19], and numerical methods [20]–[34]. However, the response characteristics of coplanar coils are much more complicated than that of coaxial coils, especially in anisotropic formation, therefore, the comprehensive research is still under development.

The analytical methods are efficient and accurate, they are suitable for 1-D problems. Among them, Green's function method (GFM) is widely used to solve electromagnetic propagation and induction problems in layered medium [8], [35]–[38], [62]. References [35], [36], [62] provided the approach for computing tool response in lossy layered formation based on the GF of layered isotropic media. Reference [8] extended the mixed potential GFM to cylindrical layered anisotropic medium and then used it to simulate the MCIL responses. Reference [37] introduced a robust formulation for the computation of tensor GF in cylindrical multilayered media under finite-precision arithmetic. Reference [38] proposed to replace point electric/magnetic current source with appropriate boundary conditions, and derived a simple expression of spectral GF in uniaxial anisotropic layered medium. Considering that the expressions of GF in the spectral domain for layered medium are different due to the various treatment of the source point and interface boundary conditions, in this article, we derive a new complete expression of GF which can be applied for the simulation of MCIL response in planar layered anisotropic medium.

Semi-analytical methods can be used to solve 2-D problems. Among them, the numerical mode matching (NMM) method is well known [17]–[19]. Its computational efficiency is higher than that of numerical method, but it cannot be applied to the cases of inclined formation or complex excitation sources (e.g., the transmitter in Fig. 1 has excitation coils T_x, T_y, and T_z in three orthogonal directions at the same time).

Numerical methods can deal with complex 3-D problems, which mainly include methods based on integral equations [20]–[25], and differential equations, e.g., finite difference method (FDM) [26] and finite element method (FEM) [26], [27], [27]–[34]. Among them, the FEM is powerful for modeling arbitrary complex structures and complex boundary conditions, so it is widely used in hydrocarbon exploration engineering. Reference [32] used vector FEM to simulate the response of induction logging, and [33] used 3-D FEM to analyze the tool response in inclined formation; [34] proposed a FEM modeling approach of EM field excited

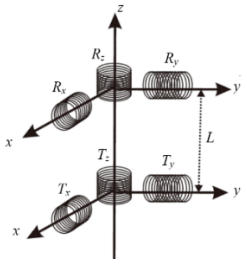

FIGURE 1. Basic structure of the coil system of the MCIL tool. Here the axis of the tool is in the z-direction, the T_z and R_z are the coaxial transmitting coil and receiving coil respectively, the T_x and T_y are the coplanar transmitting coils, the R_x and R_y are the coplanar receiving coils. L is the transmitter–receiver spacing.

by coil current source in arbitrary direction, and analyzed the IL response characteristics under pulse excitation. However, due to the large computational domain of the FEM, the number of unknown parameters to be solved is very large. To reduce the computational cost, some extension methods are introduced and have achieved remarkable results, such as the methods based on domain decomposition [39]–[44], [59], [60], and methods based on hybrid order hierarchical basis function [29], [45], [63]. In addition, another promising way is to use an appropriate meshing scheme according to the EM field distribution and geometry of the solution region [33], [43], [61], [67]. In this article, we propose a new meshing scheme based on cylindrical hexahedron elements and flexible mesh strategy for FEM simulating the 3-D MCIL problems, thus effectively reducing the unknown quantities while ensuring the accuracy.

In general, 1-D analytical methods and 2-D NMM methods are fast and accurate, but they are unsuitable for complicated cases. While numerical methods can solve complex 3-D problems, but they usually suffer from the high computational cost. Therefore, in this article we combine the analytical method and numerical method to effectively investigate the main impacting factors and response characteristics of MCIL tool. That is, for the problems that can be simplified to 1-D cases, e.g. when considering the influence of single environment on logging response, the formation can be considered as a 1-D layered model, we construct the PLAMGF method which is based on the LMGF [47] and combined with MCIL excitation source and the multilayered anisotropic formation environment, and then use it to simulate the MCIL responses, investigate the influences from shoulder bed and formation dip angle, and analyze the equivalence of tool responses in thin interbed medium and anisotropic medium. For the complicated 3-D problems where there are layered structures in both axial and radial directions, such as effects of borehole, eccentricity, and invasion on the responses (mandrel effect is not considered in this article), we use the FEM based on a proposed new meshing scheme for simulation.

The rest of this article is organized as follows. Section II gives the detailed derivations of the PLAMGF formulas. Section III introduces a new meshing scheme for FEM

simulation. Section IV presents numerical results about the following aspects: validating the PLAMGF method and the FEM meshing scheme, and using the PLAMGF method to efficiently analyze some 1-D problems including the equivalence between the tool responses in thin interbed medium and that in anisotropic medium (also called effective medium theory [56]–[58]), as well as effects of shoulder bed and formation dip on tool responses; use of FEM with new meshing scheme to analyze complicated 3-D problems including effects of borehole, eccentricity, and invasion on tool responses; investigation on the detection performances of coaxial coils and coplanar coils. Section V gives a brief conclusion.

II. GREEN'S FUNCTION FOR PLANAR LAYERED ELECTRIC ANISOTROPIC MEDIUM

The layered-medium Green's functions (LMGF) [47] was firstly proposed by Michalski and Mosing in 1997, after that, many fruitful researches have been done on the development of this method from different aspect, e.g., some focus on developing its extension method for the application in related fields, and some focus on developing the efficient algorithm of Green's function [50]–[55], [62]. In this article, we develop the extension method of LMGF and then use it to effectively solve the 1-D MCIL problems, that is, we combine the LMGF with MCIL excitation source and the multilayered anisotropic formation environment, then analyze the equivalent voltage and current of the transmission line when the excitation source (source point) and the measurement point (field point) are in different positions, and finally, a set of calculation formulas are derived. As such, the traditional LMGF is then expand to be an effective method for solving 1-D MCIL problems, we call it the PLAMGF method. The detailed derivation process is as follows.

A MCIL tool is composed of three pairs of mutually orthogonal transmitter-receiver coils. Fig. 2(a) is the schematic illustration of the MCIL tool placed in planar layered uniaxial anisotropic formation, where, the angle between the tool and the formation normal is θ, the azimuth angle is φ, the horizontal and vertical conductivities of each layer are σ_{vi} and σ_{hi} respectively, here $i = 1, 2, \cdots, N$. Considering that the transmitter and receiver coils is much smaller than the transmitter–receiver spacing, they can be safely replaced with $T_{x'}$, $T_{y'}$, $T_{z'}$ and $R_{x'}$, $R_{y'}$, $R_{z'}$ i.e., the magnetic dipoles in three directions in the tool coordinate system (x', y', z') [7], [8], [13], as shown in Fig. 2(b). Let the magnetic moments of the three transmitting dipoles be $M^T_{x'}, M^T_{y'}, M^T_{y'}$, the magnetic field produced by them at the receiving dipoles can be obtained from the following equation

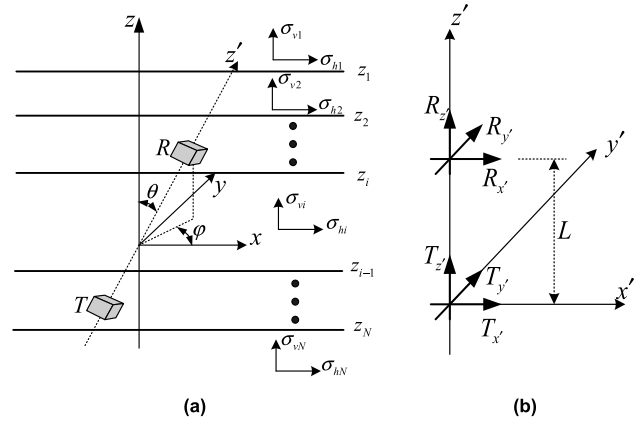

FIGURE 2. MCIL tool in planar layered anisotropic uniaxial formation. Here, (x, y, z) is the formation coordinate system, and (x', y', z') is the tool coordinate system. (a) Schematic illustration of the transmitters and receivers of a MCIL tool in a planar layered anisotropic formation. (b) Basic structure of the MCIL tool.

$$\begin{pmatrix} H_{x'} \\ H_{y'} \\ H_{z'} \end{pmatrix} = [\boldsymbol{R}]^{-1}\, \bar{\boldsymbol{G}}\, [\boldsymbol{R}] \begin{pmatrix} M^T_{x'} \\ M^T_{y'} \\ M^T_{z'} \end{pmatrix}. \tag{1}$$

where, $[\boldsymbol{R}]$ is the transformation matrix from the tool coordinate system (x', y', z') to the formation coordinate system (x, y, z)

$$[\boldsymbol{R}] = \begin{bmatrix} \cos\theta\cos\varphi & -\cos\theta\sin\varphi & \sin\theta \\ \sin\varphi & \cos\varphi & 0 \\ -\sin\theta\cos\varphi & \sin\theta\sin\varphi & \cos\theta \end{bmatrix}, \tag{2}$$

and $\bar{\boldsymbol{G}}$ is the dyadic GF in the anisotropic layered medium, which can be expressed as a matrix with nine components

$$\bar{\boldsymbol{G}} = \begin{bmatrix} G^{HM}_{xx} & G^{HM}_{xy} & G^{HM}_{xz} \\ G^{HM}_{yx} & G^{HM}_{yy} & G^{HM}_{yz} \\ G^{HM}_{zx} & G^{HM}_{zy} & G^{HM}_{zz} \end{bmatrix}. \tag{3}$$

The components of GF in Equation (3) are derived as follows. First, by converting the Maxwell equation into a scalar form, then a set of equivalent transmission line equations can be obtained based on the principle of transmission line equivalence. Related detailed derivations are shown in APPENDIX. Based on Equation (A-12) and the method given in [46], [47], the GF of current and voltage in the equivalent transmission line equations can be obtained respectively, which can be expressed in three cases as follows.

A. CASE 1: THE FIELD POINT AND THE SOURCE POINT ARE LOCATED IN THE SAME LAYER

In this case, the layer number (m) of the field point is equal to the layer number (n) of the source point, i.e., m = n, (m, n = 1, 2, . . . , N), the voltage and current are expressed as

$$\begin{aligned} V^p_i(n, z; n, z') &= \frac{Z^p_n}{2}\left[e^{ik^p_{zn}|z-z'|} + \frac{1}{D^p_n}\boldsymbol{C}_1 \cdot \boldsymbol{R}^p\right] \\ V^p_v(n, z; n, z') &= \frac{1}{2}\left[Sgn(z-z')e^{ik^p_{zn}|z-z'|} + \frac{1}{D^p_n}\boldsymbol{C}_2 \cdot \boldsymbol{R}^p\right] \\ I^p_i(n, z; n, z') &= \frac{1}{2}\left[Sgn(z-z')e^{ik^p_{zn}|z-z'|} + \frac{1}{D^p_n}\boldsymbol{C}_3 \cdot \boldsymbol{R}^p\right] \\ I^p_v(n, z; n, z') &= \frac{Y^p_n}{2}\left[e^{ik^p_{zn}|z-z'|} + \frac{1}{D^p_n}\boldsymbol{C}_4 \cdot \boldsymbol{R}^p\right], \end{aligned} \tag{4}$$

where, $Sgn(z) = \begin{cases} 1, & z > 0 \\ -1, & z < 0 \end{cases}$, $D_n^p = 1 - \overleftarrow{R}_n^p \overrightarrow{R}_n^p t_n$,

$$\begin{bmatrix} \boldsymbol{C}_1 \\ \boldsymbol{C}_2 \\ \boldsymbol{C}_3 \\ \boldsymbol{C}_4 \end{bmatrix} = \begin{bmatrix} 1 & 1 & 1 & 1 \\ 1 & -1 & 1 & -1 \\ -1 & 1 & 1 & -1 \\ -1 & -1 & 1 & 1 \end{bmatrix}, \quad \boldsymbol{R}^p = \begin{bmatrix} \overrightarrow{R}_n^p e^{ik_{zn}^p[2z_{n-1}-(z+z')]} \\ \overleftarrow{R}_n^p e^{ik_{zn}^p[(z+z')-2z_n]} \\ \overrightarrow{R}_n^p \overleftarrow{R}_n^p e^{ik_{zn}^p[2d_n+(z-z')]} \\ \overleftarrow{R}_n^p \overrightarrow{R}_n^p e^{ik_{zn}^p[2d_n-(z-z')]} \end{bmatrix},$$

and $d_n = z_{n-1} - z_n$, $t_n = e^{i2k_{zn}^p d_n}$.

Where $\overleftarrow{R}_n^p$ and $\overrightarrow{R}_n^p$ represent the generalized reflection coefficients of downward and upward respectively, they can be obtained by recursion of the following formula

$$\begin{aligned} \overleftarrow{R}_n^p &= \frac{R_{n+1,n}^p + \overleftarrow{R}_{n+1}^p t_{n+1}}{1 + R_{n+1,n}^p \overleftarrow{R}_{n+1}^p t_{n+1}} \\ \overrightarrow{R}_n^p &= \frac{R_{n-1,n}^p + \overleftarrow{R}_{n-1}^p t_{n-1}}{1 + R_{n-1,n}^p \overleftarrow{R}_{n-1}^p t_{n-1}}. \end{aligned} \tag{5}$$

where $R_{a,b}^p$ is the local reflection coefficient from the a^{th} layer to the adjacent b^{th} layer, which can be expressed as

$$R_{a,b}^p = \frac{Z_a^p - Z_b^p}{Z_a^p + Z_b^p}. \tag{6}$$

B. CASE 2: THE FIELD POINT IS BELOW THE LAYER WHERE THE SOURCE POINT IS LOCATED

In this case, the layer number (m) of the field point is larger than the layer number (n) of the source point, i.e., m>n, (m, n = 1, 2, . . . , N), the voltage and current are expressed as

$$\begin{aligned} V_{v,i}^p(m,z;n,z') &= V_{v,i}^p(m,z_n;n,z') \left\{ \prod_{k=n+1}^{m-1} \overleftarrow{T}_k^p \right\} \\ &\quad \times \frac{\left[1 + \overleftarrow{R}_m^p e^{i2k_{zm}^p(z-z_m)}\right] e^{ik_{zm}^p(z_{m-1}-z)}}{1 + \overleftarrow{R}_m^p t_m}, \\ I_{v,i}^p(m,z;n,z') &= V_{v,i}^p(m,z_n;n,z') \left\{ \prod_{k=n+1}^{m-1} \overleftarrow{T}_k^p \right\} \\ &\quad \times \frac{Y_m^p \left[-1 + \overleftarrow{R}_m^p e^{i2k_{zm}^p(z-z_m)}\right] e^{ik_{zm}^p(z_{m-1}-z)}}{1 + \overleftarrow{R}_m^p t_m}, \end{aligned} \tag{7}$$

where $\overleftarrow{T}_k^p$ is the voltage transmission coefficient expressed as

$$\overleftarrow{T}_k^p = \frac{V_{v,i}^p(z_k)}{V_{v,i}^p(z_{k-1})} = \frac{(1 + \overleftarrow{R}_k^p) e^{ik_{zk}^p d_k}}{1 + \overleftarrow{R}_k^p t_k}. \tag{8}$$

C. CASE 3: THE FIELD POINT IS ABOVE THE LAYER WHERE THE SOURCE POINT IS LOCATED

In this case, the layer number (m) of the field point is smaller than the layer number (n) of the source point, i.e., m<n, (m, n = 1, 2, . . . , N), the voltage and current are expressed as

$$\begin{aligned} V_{v,i}^p(m,z;n,z') &= V_{v,i}^p(m,z_{n-1};n,z') \left\{ \prod_{k=m+1}^{n-1} \overleftarrow{T}_k^p \right\} \\ &\quad \times \frac{\left[1 + \overleftarrow{R}_m^p e^{i2k_{zm}^p(z_{m-1}-z)}\right] e^{ik_{zm}^p(z-z_m)}}{1 + \overleftarrow{R}_m^p t_m} \\ I_{v,i}^p(m,z;n,z') &= V_{v,i}^p(m,z_n;n,z') \left\{ \prod_{k=m+1}^{n-1} \overleftarrow{T}_k^p \right\} \\ &\quad \times \frac{Y_m^p \left[-1 + \overleftarrow{R}_m^p e^{i2k_{zm}^p(z_{m-1}-z)}\right] e^{ik_{zm}^p(z-z_m)}}{1 + \overleftarrow{R}_m^p t_m}, \end{aligned} \tag{9}$$

Defining $\bar{\boldsymbol{G}}_{HM}^{mn}$ as the GF corresponding to the magnetic field in the m$^{\text{th}}$ layer which generated by the magnetic current source located in the n$^{\text{th}}$ layer, and defining $\tilde{\bar{\boldsymbol{G}}}_{HM}^{mn}$ as the spectral form of $\bar{\boldsymbol{G}}_{HM}^{mn}$, then we have

$$\tilde{\boldsymbol{H}} = <\tilde{\bar{\boldsymbol{G}}}_{HM}^{mn}, \tilde{\boldsymbol{M}}>. \tag{10}$$

When the GF of the transmission line is known, the components of the spectral GF of the magnetic field generated by the magnetic current source can be obtained by comparing (A-10) with (10).

$$\begin{aligned} &\tilde{\bar{\boldsymbol{G}}}_{HM}^{mn} \\ &= \begin{bmatrix} -\frac{k_x^2}{k_\rho^2} I_v^h - \frac{k_y^2}{k_\rho^2} I_v^e, & \frac{k_x k_y}{k_\rho^2}(I_v^e - I_v^h), & \frac{k_x}{\omega\mu_n} I_i^h \\ \frac{k_x k_y}{k_\rho^2}(I_v^e - I_v^h), & -\frac{k_y^2}{k_\rho^2} I_v^h - \frac{k_x^2}{k_\rho^2} I_v^e, & \frac{k_y}{\omega\mu_n} I_i^h \\ \frac{k_x}{\omega\mu_m} V_v^h, & \frac{k_y}{\omega\mu_m} V_v^h, & -\frac{1}{-i\omega\mu_n}\left[\frac{k_\rho^2}{-i\omega\mu_m} V_i^h - \delta(z-z')\right] \end{bmatrix}_{x,y,z} \end{aligned} \tag{11}$$

In order to transform the spectral GF in (11) into the spatial GF, the following inverse Fourier transformation is required,

$$\begin{aligned} f(\rho) &= \mathbb{F}^{-1}\left[\tilde{f}(k_\rho)\right] \\ &= \frac{1}{(2\pi)^2} \int_{-\infty}^{+\infty} \int_{-\infty}^{+\infty} \tilde{f}(k_\rho) e^{i[k_x(x-x')+k_y(y-y')]} dk_x dk_y, \end{aligned} \tag{12}$$

it has the following relationships (as shown in (14)) with the Sommerfeld integral defined in (13) [17].

$$\begin{aligned} S_n[\tilde{f}(k_\rho)] &= \frac{1}{2\pi} \int_0^{+\infty} \tilde{f}(k_\rho) k_\rho^{n+1} J_n(k_\rho \rho) dk_\rho, \\ \mathbb{F}^{-1}[\tilde{f}(k_\rho)] &= S_0[\tilde{f}(k_\rho)] \\ \mathbb{F}^{-1}[ik_x \tilde{f}(k_\rho)] &= -\cos\beta S_1[\tilde{f}(k_\rho)] \\ \mathbb{F}^{-1}[ik_y \tilde{f}(k_\rho)] &= -\sin\beta S_1[\tilde{f}(k_\rho)] \end{aligned} \tag{13}$$

$$\mathbb{F}^{-1}[k_x^2\tilde{f}(k_\rho)] = -\frac{1}{2}\left\{\cos 2\beta S_2[\tilde{f}(k_\rho)] - S_0[k_\rho^2\tilde{f}(k_\rho)]\right\}$$
$$\mathbb{F}^{-1}[k_y^2\tilde{f}(k_\rho)] = \frac{1}{2}\left\{\cos 2\beta S_2[\tilde{f}(k_\rho)] + S_0[k_\rho^2\tilde{f}(k_\rho)]\right\}$$
$$\mathbb{F}^{-1}[k_x k_y\tilde{f}(k_\rho)] = -\frac{1}{2}\sin 2\beta S_2[\tilde{f}(k_\rho)], \quad (14)$$

where $\beta = \arctan[(y-y')/(x-x')]$. By using (14) to carry out the inverse Fourier transform for (11), the components of the spatial GF in (3) can then be obtained, as shown below.

$$G_{xx}^{HM} = \frac{1}{2}\left\{\cos 2\beta S_2\left[\frac{I_v^h - I_v^e}{k_\rho^2}\right] - S_0\left[I_v^h + I_v^e\right]\right\}$$
$$G_{yy}^{HM} = -\frac{1}{2}\left\{\cos 2\beta S_2\left[\frac{I_v^h - I_v^e}{k_\rho^2}\right] + S_0\left[I_v^h + I_v^e\right]\right\}$$
$$G_{zz}^{HM} = S_0\left[k_\rho^2 V_i^h\right] \quad G_{xy}^{HM} = -\frac{1}{2}\sin 2\beta S_2\left[\frac{I_v^e - I_v^h}{k_\rho^2}\right] = \tilde{G}_{yx}^{HM}$$
$$G_{xz}^{HM} = \cos\beta S_1\left[\frac{-I_i^h}{i\omega\mu_n}\right] \quad G_{zx}^{HM} = \cos\beta S_1\left[\frac{-V_v^h}{i\omega\mu_m}\right]$$
$$G_{yz}^{HM} = \sin\beta S_1\left[\frac{-I_i^h}{i\omega\mu_n}\right] \quad G_{zy}^{HM} = \sin\beta S_1\left[\frac{-V_v^h}{i\omega\mu_m}\right], \quad (15)$$

In this article, direct numerical integration is conducted for computing the Sommerfeld integral in (15). Since the formation is a lossy medium, the integration along the real axis will not meet the branch points and branch cuts. Where, the branch points are the points corresponding to the value of k_ρ in the complex k_ρ-plane when $k_z = \sqrt{k_t^2 - \lambda k_\rho^2} = 0$, i.e., $k_\rho = \pm\sqrt{k_t^2/\lambda}$ in the complex k_ρ-plane [17]. The branch cuts are the paths of k_ρ when $k_t^2 - \lambda k_\rho^2 = R$ (R is a positive real number), that is, the paths corresponding to $k_\rho = \sqrt{(k_t^2 - R)/\lambda}$ (when R: $0 \to \infty$) in the complex k_ρ-plane [17].

III. A NEW MESHING SCHEME FOR FEM

The 3-D numerical modeling for MCIL problems, such as FEM modeling, is a big challenge, that is because the modeling process usually produces a large number of unknowns and involves solving FEM large linear equations, hence leads to huge memory requirement and CPU time (i.e., the sum of the time for filling the coefficient matrix of linear equations and the time for solving linear equations). Especially, in order to obtain satisfactory accuracy, it is theoretically need to mesh the whole solution domain with enough fine (i.e. dense) grid, which will produce huge unknown quantity and computational load. Therefore, an effective meshing scheme is necessary. The design of meshing scheme has a great influence on both the accuracy and efficiency of FEM modeling, the reason is that: firstly, the mesh must be as consistent as possible with the geometry of the solution domain and the boundary shape, so as to reduce the numerical discretization error as much as possible, thus ensuring the accuracy of FEM modeling; secondly, the meshing scheme should help to generate as small unknown quantity as possible while keeping the satisfactory accuracy, so as to reduce the memory requirement as well as the CPU time on solving large linear equations (this time consumption is usually 80% or even more of the total time of the whole process of FEM modeling). Therefore, for the 3-D modeling of MCIL problems, an effective meshing scheme should be developed [29], [33], [43], [61], [63], [67].

In this section, a new flexible meshing scheme is presented to effectively reduce the FEM computational cost while maintaining the satisfactory accuracy, it includes two aspects: one is the use of cylindrical hexahedron element (as shown in Fig.3(a)), the other is the flexible meshing strategy combined with domain decomposition.

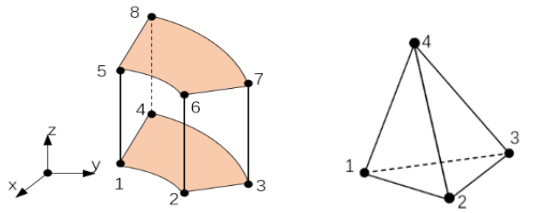

(a) Cylindrical hexahedral element. (b) Tetrahedra element.

FIGURE 3. Illustration of the cylindrical hexahedron element and conventional tetrahedra element.

Firstly, compared with the commonly used tetrahedral element [33], [61] (as shown in Fig.3(b)), the proposed cylindrical hexahedron element [29] is more suitable for MCIL simulation. The main advantage of using cylindrical hexahedron is that, in the case of the same mesh element size, the number of hexahedron elements required is much less than that of tetrahedral elements, hence can effectively reduce the unknowns and accordingly reduce the memory consumption and CPU time for solving FEM linear equations. Besides, it can provide enough flexibility in modeling of the geometry with pronounced curvature, such as the borehole wall or boundary of invasion zone, hence can reduce the numerical discretization error, and improve the accuracy of FEM modeling. Although the accuracy may be improved by using some curved tetrahedron element, a large number of unknowns still cannot be avoided.

Secondly, in order to further reduce the memory consumption and CPU time, a flexible meshing strategy combined with domain decomposition is proposed. Here, we take a basic MCIL model as shown in Fig. 4(a) as an example to describe the proposed flexible meshing strategy. It should be noted that, in practice, only one coplanar coil pair is needed since it can be used as the other coplanar coil pair orthogonal to it when it is rotated 90 degrees along the z-axis. As shown in Fig. 4(b)-(d), based on the characteristics of the EM field, the solution domain is divided into two subdomains: the area within the borehole ($\Lambda 1$) and the area outside the borehole ($\Lambda 2$). In $\Lambda 1$, the dense mesh is used because the EM field here changes fast, especially for the coils and the area close to them, and also the field in $\Lambda 1$ contributes a lot to the final measured data. In $\Lambda 2$, the sparse mesh (gradually sparse in radial direction and z-direction) is used because the EM field

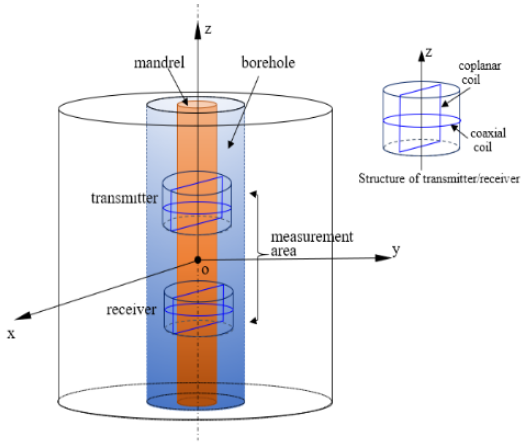

(a) Basic structure of MCIL tool and formation model.

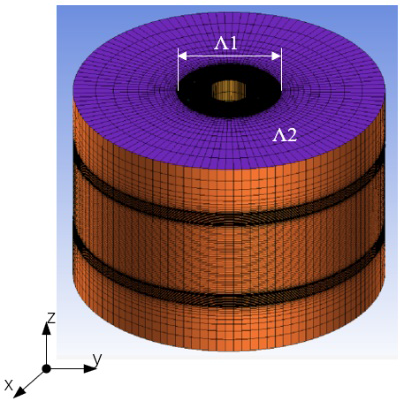

(b) The meshing result based on cylindrical hexahedron elements.

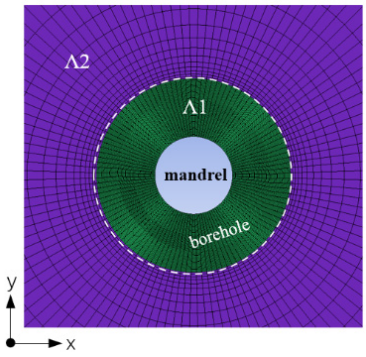

(c) From a cross sectional view (xoy-plane).

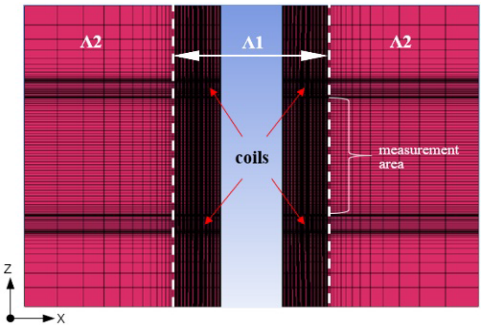

(d) From a longitudinal sectional view (xoz-plane).

FIGURE 4. Illustration of the proposed meshing scheme. The white dotted line represents the boundary line, Λ1 and Λ2 represent the subdomains within and outside the borehole, respectively.

here changes slowly and has relatively uniform distribution, and also, its contribution to the final measurement data is smaller than that of Λ1. As such, the number of mesh elements needed can be as few as possible, so the total unknown quantity can be effectively reduced while maintaining the satisfactory accuracy. Then the fields in Λ1 and Λ2 can be solved independently by parallel computation, and the solutions are coupled at the boundary through the transmission condition [64]–[66] without the need for the grid lines to be continuous, through which the computational cost can be further reduced.

Moreover, we specially design the mesh to be uniform in z-direction for the measurement area, the advantage of this way is, when the positions of the measurement points are moved (along the z-direction), only the positions of the transmitter and the receiver need to be moved accordingly, while no need to re-mesh again, hence can save a lot of time for mesh generation, and so can further improve the efficiency of FEM modeling.

IV. NUMERICAL EXAMPLES AND DISSUSSIONS

In this section, we firstly validate the effectiveness of the PLAMGF method and the flexible meshing scheme for FEM analysis. Then, the PLAMGF method is used to analyze some 1-D problems, such as the equivalence between the tool responses in thin interbed medium and that in anisotropic medium, effects of shoulder bed and formation dip on tool responses. Moreover, we use the FEM along with our new meshing scheme to analyze some complicated 3-D problems, such as effects of borehole, eccentricity, and invasion on tool responses. Besides, we also investigate the detection performances of coaxial coils and coplanar coils.

A. CALCULATION OF APPARENT CONDUCTIVITY

The apparent conductivities in three directions (x, y, z) can be calculated by equation (16) [6]. Where, the responses of coplanar coils, σ^a_{xx} and σ^a_{yy}, represent the vertical apparent conductivities of the formation, and the response of coaxial coils σ^a_{zz} represents the horizontal apparent conductivity of the formation.

$$\sigma^a_{xx} = \frac{8\pi L}{\omega\mu}\mathrm{Im}(H_{xx}), \quad \sigma^a_{yy} = \frac{8\pi L}{\omega\mu}\mathrm{Im}(H_{yy}),$$
$$\sigma^a_{zz} = \frac{4\pi L}{\omega\mu}\mathrm{Im}(H_{zz}), \tag{16}$$

where L is the transmitter-receiver spacing.

B. VALIDATION OF THE PLAMGF METHOD

In this subsection, the PLAMGF method and FEM are used to calculate the response of three orthogonal coils in PLAM. Since the effectiveness of the FEM has been verified, the correctness of PLAMGF method can be evaluated by comparing the simulation results of the two methods. In this numerical test, the structure of formation model and coil system are shown in Fig. 5, where, σ_h and σ_v represent horizontal and

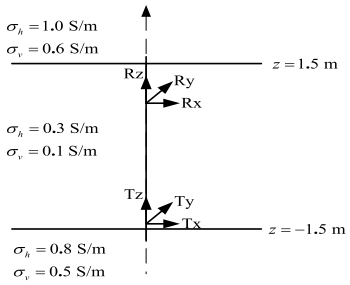

FIGURE 5. Three-layer anisotropic formation and triaxial transmitting-receiving coil system.

vertical formation conductivities of each layer respectively (corresponding to the two dashed lines in Fig. 6). Both the transmitting and receiving coils have three orthogonal field components. The $L = 0.8$m, $f = 20\ kHz$, and the number of cylinder hexahedron mesh elements is $N_\rho \times N_\varphi \times N_z = 28 \times 20 \times 88$. The numerical results are shown in Fig. 6, the symbols "G" and "FEM" represent the apparent conductivity curves calculated by PLAMGF and FEM, respectively. Considering that the model is axisymmetric, σ^a_{xx} is equal to σ^a_{yy}, so the curve of σ^a_{yy} is not provided. From Fig. 6, it can be seen that the results of the two methods are in good agreement, which proves the correctness of the PLAMGF method.

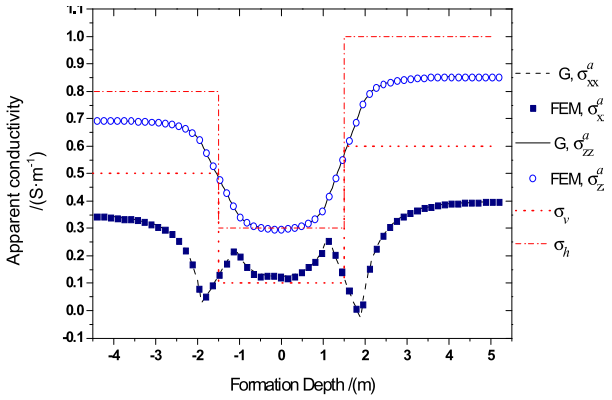

FIGURE 6. Comparison between the results of PLAMGF method and FEM.

C. VALIDATION OF THE FLEXIBLE MESHING SCHEME

In this subsection, the advantages of the proposed flexible meshing scheme will be verified by comparing with other conventional schemes. A formation model as shown in Fig. 4(a) is taken as an example, which composed of metal mandrel, coil, borehole (with $\sigma_{\rm m} = 5$S/m) and original formation (with $\sigma_{\rm f} = 0.1$ S/m). The platform is 64 core Dell server and is calculated by OpenMP parallel strategy. Table 1 shows the comparison of accuracy and efficiency of FEM with different meshing schemes for a MCIL problem as shown in Fig. 4(a). Where, CASE 1 represents the case of using the meshing scheme proposed in this article. CASE 2 represents the case of using the same flexible meshing strategy in CASE 1, but using the conventional tetrahedral element (the element size is the same as that in CASE 1). CASE 3 represents that a sparse and uniform mesh based on cylindrical hexahedron elements for the whole domain (i.e., without domain decomposition), and CASE 4 represents that a dense and uniform mesh based on cylindrical hexahedron elements for the whole domain. In Table 1, the "Filling time" means the time for filling the coefficient matrix of FEM linear equations, and the "Solving time" means the time for solving FEM linear equations. The "Computation accuracy" is defined as the maximum error relative to analytical solution, so the smaller value means the better computation accuracy.

TABLE 1. Comparison of the accuracy and efficiency of FEM analyzing MCIL problems. Where the symbol '∗' indicates that the computation is terminated due to a memory overflow.

	CASE 1	CASE 2	CASE 3	CASE 4
Unknown number	209,375	518,643	72,652	4,370,368
Filling time (s)	176	430	63	*
Solving time (s)	233	692	67	*
Peak memory requirements (GB)	3.12	8.96	1.33	*
Computation accuracy	3.02%	4.30%	26.34%	<3.02%

From Tab.1 we can see that, the proposed meshing scheme (CASE 1) outperforms all the other schemes. In CASE 2, the number of unknown is much more than that of CASE 1 due to the use of tetrahedral elements, which leads to the computational cost much higher than that of CASE 1. In addition, as mentioned before, due to the existence of the planar sides, the tetrahedral is not very suitable for the geometry with curved surface such as the borehole wall, so the computation accuracy is not as good as that of CASE 1. CASE 3 does not use the proposed flexible meshing strategy, but treats $\Lambda 1$ and $\Lambda 2$ equally, and uses a uniform sparse mesh for the overall solution domain, through which, the number of mesh elements are reduced, thus reducing the unknown quantity and computational cost. However, since the mesh on $\Lambda 1$, where the EM field changes rapidly and has great influence on measurement data, is not fine (i.e. dense) enough, hence results in poor simulation accuracy. On the contrary, the scheme of CASE 4 uses a uniform dense mesh for the overall solution domain, which leads to a huge number of unknowns and then causing the memory overflow, so the calculation is terminated. Although the computation process is not completed, we can still safely draw a conclusion according to the huge number of unknowns that, the meshing scheme of CASE 4 can obtain better computation accuracy than all the other three schemes, however, its memory consumption is the highest, and apparently this tremendous computation cost makes this scheme not feasible for practical use.

D. ANALYSIS OF THE EQUIVALENCE BETWEEN THE MCIL TOOL RESPONSE IN THIN INTERBED MEDIUM AND THAT IN ANISOTROPIC MEDIUM

In the construction of experimental wells, it is usually difficult to construct the anisotropic layer. If we can find an equivalent

and easy to implement model by numerical simulation, that will provide a new approach for the construction of experimental wells. Wang *et al.* have studied the equivalence of lateral logging response in thin interbed medium and that in anisotropic medium [48], but which is based on direct current (DC) logging. In this article, we use the PLAMGF method to analyze the equivalence of MCIL response in these two kinds of formation. The formation models shown in Fig. 7 (a) and Fig. 7 (b) are considered. In Fig. 7(a), the middle area is a thin interbed layer with conductivity of 0.1 S/m and 1.0 S/m, respectively. The total thickness of the middle layer is 4m, and the conductivities of both the two side layers are 1.0 S/m. Fig. 7 (b) is the anisotropic model derived from model in Fig. 7 (a) based on the principle of series-parallel equivalent circuit. The horizontal formation conductivity of the middle layer is $\sigma_h = 0.55$S/m and the vertical conductivity is $\sigma_v = 0.1818$S/m.

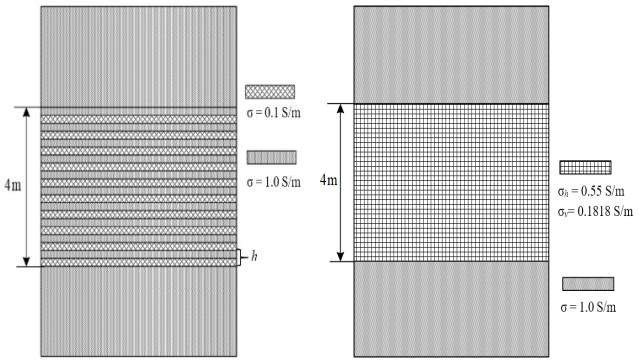

(a) Thin interbed model. (b) Anisotropic model.

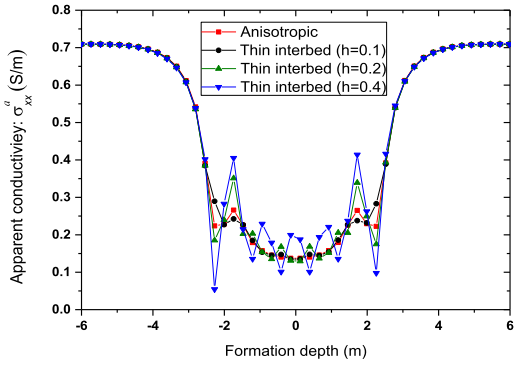

(c) Vertical apparent conductivity σ^a_{xx} with respect to the formation depth.

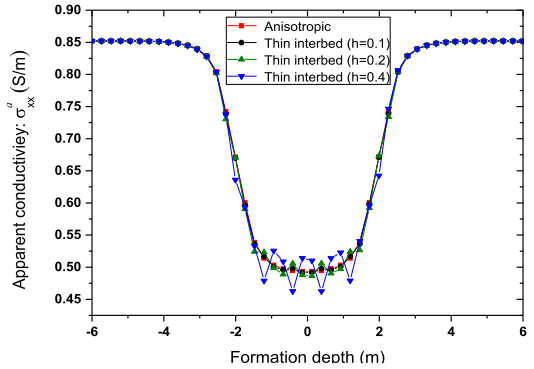

(d) Horizontal apparent conductivity σ^a_{zz} with respect to the formation depth.

FIGURE 7. Structures of the thin interbed model and anisotropic model, and the comparison of tool responses in them, when h = 0.1m, 0.2m, and 0.4m respectively.

In order to study the equivalence between the models in Fig. 7 (a) and Fig. 7 (b), we set the thickness of single layer in Fig. 7 (a) to be h = 0.1m, 0.2m, and 0.4m respectively. Fig. 7(c) and Fig. 7 (d) show the horizontal and vertical apparent conductivity curves corresponding to different thickness of thin layer respectively. It can be seen from Fig. 7 (c) and Fig. 7 (d) that when h = 0.4m, the amplitude fluctuation of response curves are relatively large, especially the σ^a_{xx} curve of coplanar coil (Fig. 7 (c)). We can also see that, when h is set to 0.1m, the tool responses are in good agreement with that in the anisotropic formation, so this kind of thin interbed layered model can be equivalent to the anisotropic model. This result is consistent with the conclusion based on lateral logging model in [48]. This example indicates that, regardless of induction logging or direct current (DC) logging, when the thickness of the single layer is less than 0.1m, the tool response in the thin interbed medium can be considered equivalent to that in the anisotropic medium. This simulation result is useful for the design of MCIL experimental well, because it proves that the anisotropic medium can be replaced by the thin interbed medium, and the latter is easy to implement in engineering, and the cost is not high.

E. EFFECTS OF SHOULDER BED

In order to analyze the effects of shoulder bed on MCIL responses in the target layer, we use a three-layer formation model. The horizontal and vertical formation conductivities of the upper and lower shoulder bed are set to $\sigma_h = 1.0$S/m and $\sigma_v = 1.0$S/m respectively, and those of the target layer (i.e., the middle layer) are set to $\sigma_h = 0.5$S/m and $\sigma_v = 0.1$S/m, respectively. The effects of the shoulder bed on MCIL tools are analyzed by changing the thickness of the target layer. In this example, we set the thickness to be h = 6.0m, 3.0m, 1.0m, and 0.5m, respectively. The vertical and horizontal apparent conductivity curves simulated by PLAMGF method are shown in Fig. 8(a) and Fig. 8(b), respectively.

It can be seen from Fig. 8 that the influence of the upper and lower shoulder bed on the response of coplanar coils (Fig. 8(a)) is greater than that on the coaxial coils (Fig. 8(b)). In Fig. 8(a), there are characteristic "horn" [49] at the interface of layers, that is because the induced current normal to the layer boundary leads to the accumulation of electrical charge at bed boundaries. The thinner the target layer is, the sharper the horn is, this characteristics is helpful to improve the bed-resolution ability of the tool although it may bring some interference to the data interpretation. In addition, when h is small, both the σ^a_{xx} and σ^a_{zz} of the target layer

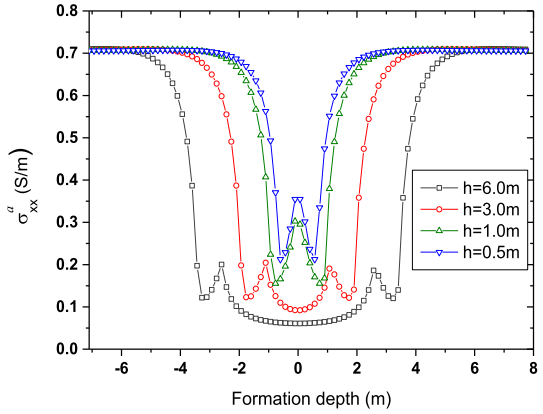

(a) Vertical apparent conductivity σ^a_{xx} with respect to the formation depth.

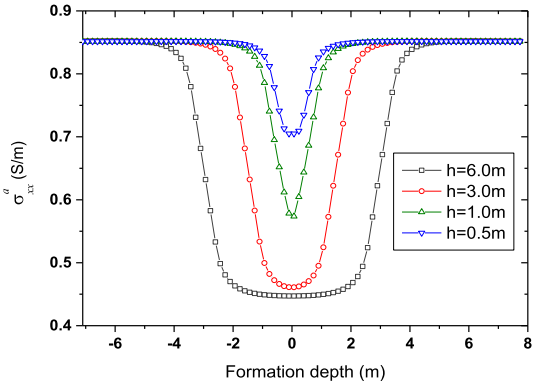

(b) Horizontal apparent conductivity σ^a_{zz} with respect to the formation depth.

FIGURE 8. Apparent conductivities in a three-layer formation model with different thickness of target layer.

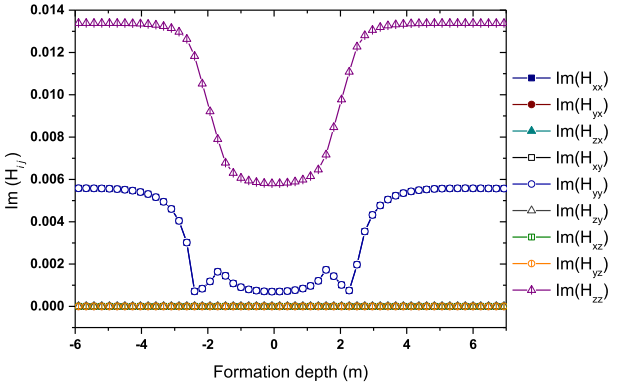

(a) Formation dip $\theta = 0^o$.

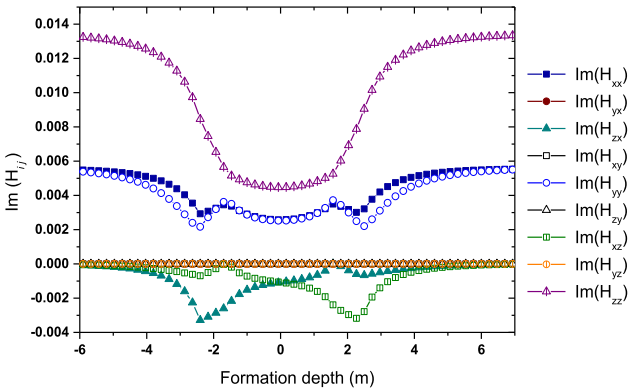

(b) Formation dip $\theta = 60^o$.

FIGURE 9. Tool responses of nine magnetic components in a three-layer formation.

deviates from the true formation conductivities σ_v and σ_h due to the effects of the shoulder bed.

F. EFFECTS OF FORMATION DIP

In order to investigate the effects of formation dip, here, we take the MCIL responses in vertical and deviated well for example, and a three-layer formation model is used. The upper and lower layers are set to be isotropic with conductivity of 1.0S/m, while the middle layer is set to be anisotropic with horizontal and vertical conductivities of $\sigma_h = 0.4$S/m and $\sigma_v = 0.1$S/m respectively, the azimuth angle of the tool axis relative to the x-direction is set to $\varphi = 0^o$. We investigate the measured nine magnetic field components H_{ij} $(i, j = \{x, y, z\})$ when the dip angles between tool axis and formation normal are $\theta = 0^o$ and $\theta = 60^o$ respectively, where, H_{ij} represents the field emitted by the j-direction magnetic dipole (coil) and received by the i-direction dipole (coil). H_{ij} represents the principal-components (when $i = j$), and the cross-components (when $i \neq j$), respectively. Fig. 9 shows the imaginary part of the H_{ij} (Im(H_{ij})) with respect to the formation depth.

From Fig. 9 (a) we can see that when the formation dip $\theta = 0°$ (the vertical well case), all the cross-components are zero, and the two curves corresponding to xx- and yy- components are completely coincident. However, when the formation dip $\theta = 60°$ (deviated well case), as shown in Fig. 9 (b), the two curves corresponding to xx- and yy-components are no longer coincident, and they are smoother than those in the case of vertical well ($\theta = 0°$). In addition, in Fig. 9(b), the xz- and zx- cross components are no longer equal to zero, and they are very sensitive to the formation dip. this characteristic can be helpful for the measurement of formation dip.

G. EFFECTS OF BOREHOLE

The effects of borehole on the MCIL tools mainly depends on the factors of borehole radius, operating frequency, borehole mud conductivity (σ_m), and formation conductivity (σ_f). Usually the borehole radius and the operating frequency are relatively fixed, so their influences are relatively stable. Therefore, we focus on the FEM analysis of the borehole effects with respect to the ratio of borehole conductivity to formation conductivity, i.e., σ_m/σ_f. The ratio of the measured apparent conductivities with borehole and without borehole is used to evaluate the borehole effects, where, the horizontal and vertical apparent conductivities without borehole are expressed as $\sigma^a_{zz,0}$ and $\sigma^a_{xx,0}$ respectively, and those with borehole are expressed as σ^a_{zz} and σ^a_{xx} respectively. That is,

the borehole effects are evaluated by $\sigma^a_{zz}/\sigma^a_{zz,0}$ in horizontal direction and $\sigma^a_{xx}/\sigma^a_{xx,0}$ in vertical direction, respectively. The more the ratio deviates from 1, the greater the borehole effect. In this simulation, the borehole radius is set to 0.1m, the formation is homogeneous with conductivities of $\sigma_f = 0.01$S/m, 0.05S/m, 0.1S/m, and 0.5S/m, respectively, the transmitter-principal receiver spacing is set to 80 cm (31.50 in). By changing σ_m, the curves of borehole effects on the horizontal and vertical apparent conductivities with contrast ratio σ_m/σ_f can be obtained, as in shown in Fig. 10.

From Fig. 10, we can see that, when $\sigma_m/\sigma_f < 1$, σ^a_{zz} is not influenced by borehole (i.e., $\sigma^a_{zz}/\sigma^a_{zz,0} = 1$), whereas σ^a_{xx} is greatly influenced, but the borehole effects (i.e., degree of $\sigma^a_{xx}/\sigma^a_{xx,0}$ deviates from 1) are less than 21%. When $\sigma_m/\sigma_f > 1$, both σ^a_{zz} and σ^a_{xx} are affected by borehole, and the effects increase with increasing of σ_m/σ_f. When $1 < \sigma_m/\sigma_f < 10$, the borehole effects on σ^a_{zz} are less than 16%, while those on σ^a_{xx} are up to 33%. When $\sigma_m/\sigma_f > 10$, the borehole effects on σ^a_{zz} and σ^a_{xx} are great, and the latter is still greater. In addition, for a same σ_m/σ_f value, the borehole effects on tool responses in high conductivity formation are more serious than those in low conductivity formation.

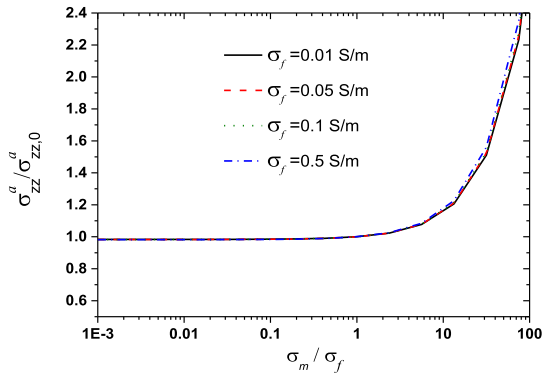

(a) Borehole effects on the horizontal apparent conductivities.

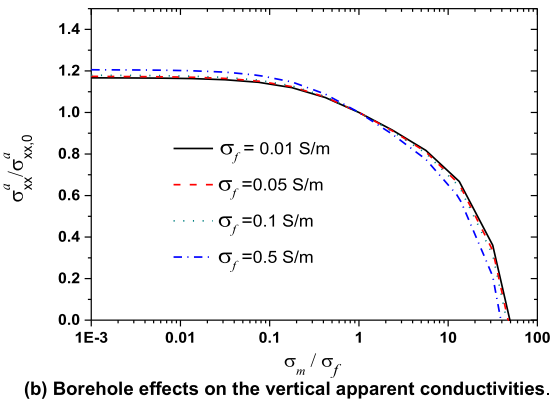

(b) Borehole effects on the vertical apparent conductivities.

FIGURE 10. Borehole effects with respect to σ_m/σ_f, $\sigma_f = 0.01$S/m, 0.05S/m, 0.1S/m, and 0.5S/m.

In general, when $\sigma_m/\sigma_f < 100$, the borehole effects on coplanar coil responses (σ^a_{xx}) are greater than that of coaxial coil responses (σ^a_{zz}), even in the case of low σ_m (the resistive borehole mud case), the borehole effects cannot be ignored.

H. EFFECTS OF TOOL ECCENTRICITY

In deviated or horizontal wells, the tool axis usually deviates from the wellbore axis because of the weight of the tool. Due to the loss of symmetry, the problem can no longer be simplified as a 1-D model, so we use the FEM based on our meshing scheme to study the effects of eccentricity on tool response. In this simulation, two formation models with borehole are investigated respectively. The radius of borehole is 0.15m, the formation is isotropic with $\sigma_f = 0.1$S/m, and the borehole mud are water-based (conductive mud) with $\sigma_m = 1.0$S/m, and oil-based (resistive mud) with $\sigma_m = 0.001$S/m, respectively. It is assumed that the tool is parallel with the borehole axis, and its eccentricity is in the x-direction. Fig. 11 shows the tool responses σ^a_{ij} $(i, j = \{x, y, z\})$ in the two formation models with respect to the eccentric distance. It can be seen from Fig. 11 that, for the water-based mud case, the eccentricity in the x-direction has a great effect on the coplanar coils in the y-direction, but that has small effect on the other coils in z- or x-directions. However, for the oil-based mud case, eccentricity has little effects on the coils in all three directions.

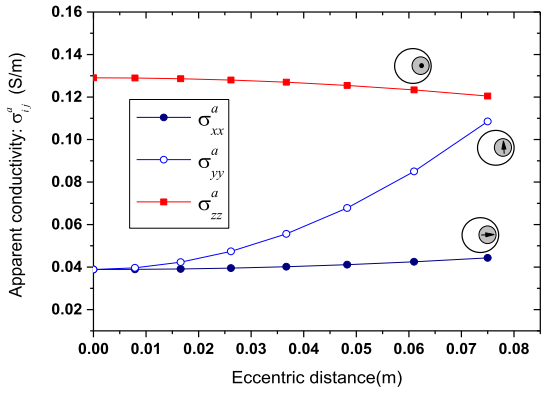

(a) In the water-based mud (conductive mud), $\sigma_m = 1.0$S/m.

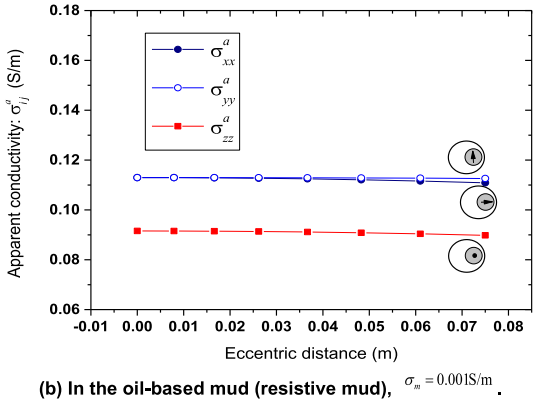

(b) In the oil-based mud (resistive mud), $\sigma_m = 0.001$S/m.

FIGURE 11. Apparent conductivities $\sigma^a_{xx}, \sigma^a_{yy}, \sigma^a_{zz}$ in three directions with respect to the eccentricity distance.

I. EFFECTS OF INVASION

1) EXAMPLE 1

It is assumed that the invaded zone is a step-type, two cases are considered. The one is with invaded zone of

high-resistance (high-invasion for short), where the conductivities of the formation and borehole are $\sigma_f = 1.0$S/m and $\sigma_m = 0.001$S/m, respectively, and the conductivity of the invaded zone is $\sigma_{xo} = 0.1$S/m. The other is with invaded zone of low-resistance (low-invasion), where the conductivities of the formation and borehole are $\sigma_f = 0.1$S/m and $\sigma_m = 1.0$S/m, respectively, and the conductivity of the invaded zone is $\sigma_{xo} = 0.5$S/m. In this simulation, the borehole environment is no longer 1-D, so we use FEM for analysis. Fig. 12 shows the tool responses σ^a_{ij} $(i, j = \{x, y, z\})$ in two cases with respect to the depth of invasion. As shown in Fig. 12(a), in high-invasion case, the response of coaxial coils (σ^a_{zz}) usually decreases with increasing of invasion depth, whereas the response of coplanar coil (σ^a_{xx}) exhibits very different characteristics, i.e., when the depth of invaded zone is shallow, σ^a_{xx} increases with invasion depth, but when the depth of invasion is deep, σ^a_{xx} decreases with invasion depth. On the other hand, as shown in Fig. 12(b), in low-invasion case, both the characteristics of σ^a_{zz} and σ^a_{xx} are opposite to those in high-invasion case.

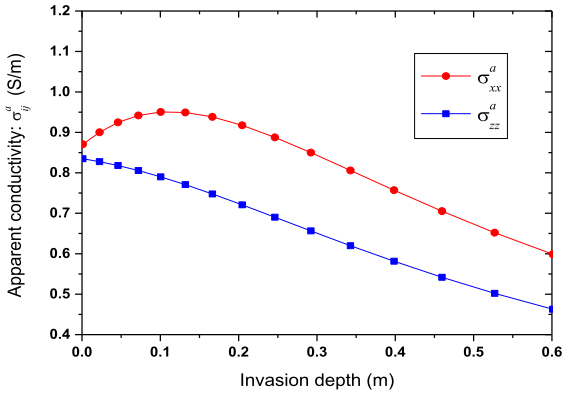

(a) High-invasion case, $\sigma_m = 0.001$ S/m, $\sigma_{xo} = 0.1$ S/m, and $\sigma_f = 1.0$S/m.

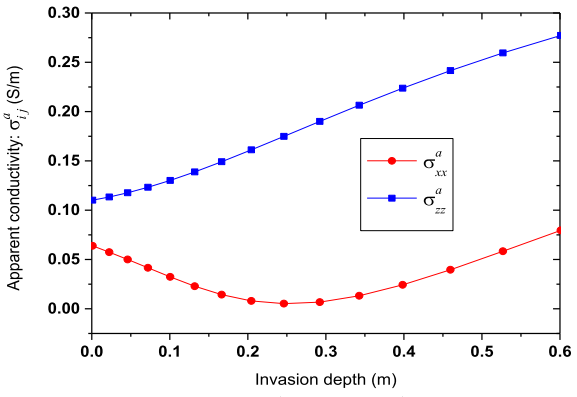

(b) Low-invasion case, $\sigma_m = 1.0$ S/m, $\sigma_{xo} = 0.5$ S/m, and $\sigma_f = 0.1$ S/m.

FIGURE 12. Apparent conductivities with respect to the invasion depth.

In general, when the depth of the invasion is shallow, the effects of the invasion on the coplanar coils is opposite to that on the coaxial coils, while when the invasion depth is deep, the effects on coplanar coils is consistent with that on coaxial coils. The reason why the response curve of coplanar coil is not monotonous is that the induced current excited by coplanar coil is in the direction of concentric circle which is coaxial with it (x-direction or y-direction), so it may cross the boundary of invasion zone, which will cause some nonlinear effects and make the response non monotonic. However, the induced current excited by coaxial coil is in the direction of concentric circle centered on z-direction, and it will not cross the boundary of invasion zone, so its response curve is monotonous.

2) EXAMPLE 2

Another four-layer formation model with borehole and invasion zone is considered. The formation is anisotropic, σ_v and σ_h of each layer are shown in Fig. 13(a). In high-invasion case, we set $\sigma_m = 0.001$ S/m, $\sigma_{xo,1} = 0.06$ S/m, and $\sigma_{xo,2} = 0.01$ S/m respectively; in low-invasion case, we set $\sigma_m = 2.0$ S/m, $\sigma_{xo,1} = 0.6$ S/m, and $\sigma_{xo,2} = 0.4$ S/m, respectively.

The tool responses with respect to the formation depth are shown in Fig. 13 (b) and Fig. 13 (c). For comparison, the results without borehole and invasion are also provided.

As mentioned in Subsection IV-G and Fig. 10(a), in the case of high-invasion, the effects of borehole alone on σ^a_{zz} is very small. However, as shown in Fig. 13 (b), when there is invasion, the line-2 moves down a lot relative to line-4. This is because in the case of high-invasion, the conductivities of the borehole mud (σ_m) and the invaded zone ($\sigma_{xo,1}$ and $\sigma_{xo,2}$) are lower than that of the formation(σ_f), that makes the response of the coaxial coil (σ^a_{zz}, line-2) much lower than that without borehole and invasion (σ^a_{zz}, line-4); whereas, that makes the response of the coplanar coil (σ^a_{xx}, line-1) much higher than that without borehole and invasion (σ^a_{xx}, line-3). On the contrary, in the case of low resistance invasion, as shown in Fig. 14(c), σ^a_{zz} (line-2) is higher than σ^a_{zz} (line-4), and σ^a_{xx}(line-1) is lower than σ^a_{xx}(line-3).

J. DETECTION PERFORMANCE OF COAXIAL COILS AND COPLANAR COILS

In this subsection, the detection performances of coaxial coils and coplanar coils are investigated, including the detection performances of formation anisotropy, radial detection depth and bed resolution.

1) PERFORMANCE OF DETECTION FORMATION ANISOTROPY

In order to investigate the resolution of coplanar and coaxial coils to formation anisotropy, a three-layer formation model is used in this simulation. The middle layer (target layer) is anisotropic with horizontal and vertical conductivities of $\sigma_h = 0.5$S/m and $\sigma_v = 0.05$S/m respectively. The upper and lower layers are isotropic with conductivity of 0.5S/m. The operating frequency is $f = 20$kHz, and the transmitter-receiver spacing is L = 80 cm (31.50 in). Fig. 14 shows the measured apparent conductivities with respect to the formation depth. It can be seen from Fig.14 that

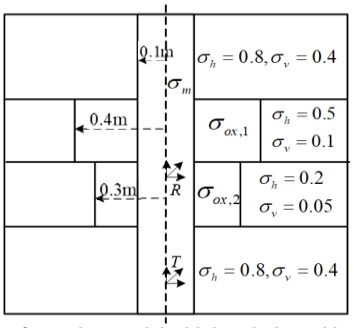

(a) Four-layer formation model with borehole and invaded zone.

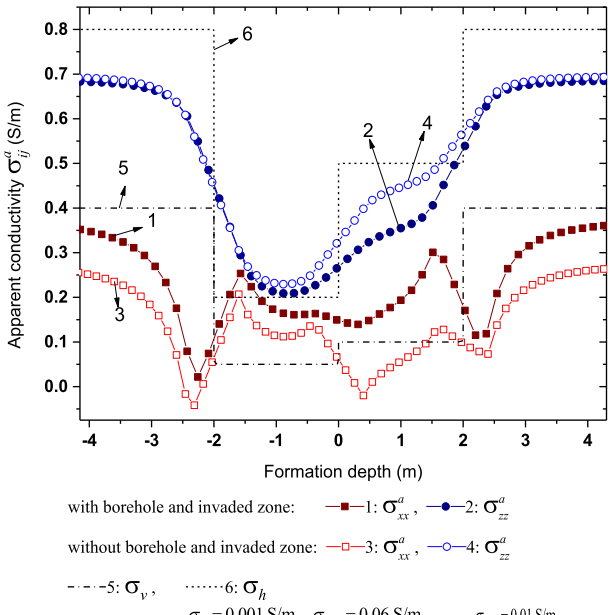

(b)High-invasion case, $\sigma_m = 0.001$ S/m, $\sigma_{xo,1} = 0.06$ S/m, and $\sigma_{xo,2} = 0.01$ S/m.

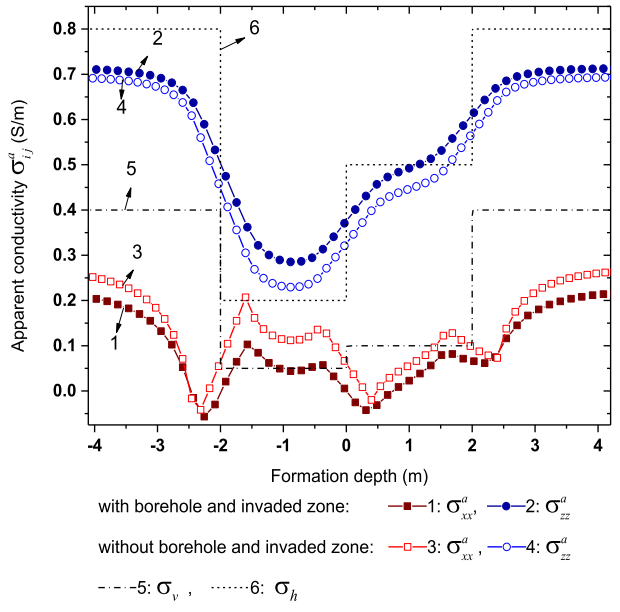

(c) Low-invasion case, $\sigma_m = 2.0$ S/m, $\sigma_{xo,1} = 0.6$ S/m, and $\sigma_{xo,2} = 0.4$ S/m.

FIGURE 13. Four-layer formation model with borehole and invade zone, and the tool responses under different invasion cases.

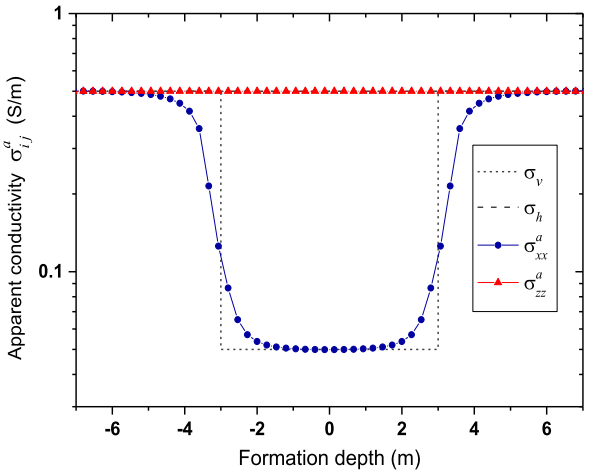

FIGURE 14. Apparent conductivities with respect to the formation depth, the target layer is anisotropic with $\sigma_h = 0.5S/m$ and $\sigma_v = 0.05S/m$.

the response σ^a_{zz} of the coaxial cools is not sensitive to σ_v of the target anisotropic layer, but the response σ^a_{xx} of the coplanar coils can be very sensitive to σ_v, therefore, the MCIL tool can detect the formation anisotropy of the target layer.

2) PERFORMANCE OF RADIAL DETECTION DEPTH

Radial detection depth (or detection depth for short, noted as D) indicates the radial measuring range of logging tools, that is, the depth of EM wave penetrating the formation. In the actual measurement environment, invasion is inevitable due to the existence of drilling mud and formation fluid. Therefore, the deeper the EM wave penetrates the formation, the closer the measurement results are to the true conductivity of the undisturbed original formation. To calculate the detection depth D, we first define a radial geometric factor. It is assumed that there are two layers of medium in radial direction starting from borehole boundary, i.e., the invaded zone and undisturbed formation zone, besides, the formation thickness in z-direction is infinite, then the radial geometric factor J_ρ is defined as follows [71]

$$J_\rho = \frac{\sigma_a - \sigma_t}{\sigma_{xo} - \sigma_t}. \tag{17}$$

where, σ_{xo} is the conductivity of invaded zone, σ_t is the true conductivity of undisturbed formation, and σ_a is the apparent conductivity. It should be noted that, without skin effect correction, the value of σ_a will deviate from the real value due to skin effect, so in (17), the σ_a should be the apparent conductivity after skin effect correction. It is obvious that J_ρ is related to the conductivity of the invasion zone, the invasion depth (i.e., radius of invaded zone) and the conductivity of the undisturbed formation. Based on (17) we can define the detection depth D in the following process: first, keeping σ_{xo} and σ_t unchanged, assuming the radius of the invaded zone is infinite, as such σ_a is equal to σ_{xo}, and J_ρ is equal to 1;

next, assuming there is no invasion, as such σ_a is close to σ_t, and J_ρ is close to 0; finally, adjusting the invasion depth so that $J_\rho = 0.5$, then the corresponding invasion depth can be defined as the detection depth D. Here, in accordance with industrial practice, the following assumptions are made when calculating D: the formation is isotropic, its thickness is infinite, that is to say, there is no axial stratification and no borehole, and step invasion model is adopted.

In this simulation, we calculate D at several operating frequencies: $f = 10$ kHz, 20 kHz, 40 kHz, 100 kHz, 160 kHz, and 220 kHz respectively. Where, $\sigma_{xo} = 0.1$ S/m, $\sigma_t = 0.01$ S/m, the transmitter-principal receiver spacing and the transmitter-compensator spacing are 160 cm (63.00 in) and 100 cm (39.37 in), respectively. The detection depths of coaxial coil and coplanar coil are shown in Fig. 15. For each curve in Fig. 15, when $J_\rho = 0.5$, the corresponding value of the abscissa is just the D. In order to be distinguished, D is expressed as D_*, where '$*$' represents the corresponding frequency. From Fig. 15 we can see that, the D_* decreases with increasing frequency; besides, the D_* of coplanar coil is deeper than that of coaxial coil at same f, and the range of D_* of coplanar coil is 2.3-3.7 m, while that of coaxial coil is 1.4-1.9 m. So, the coplanar coil has better radial detection depth than the coaxial coil.

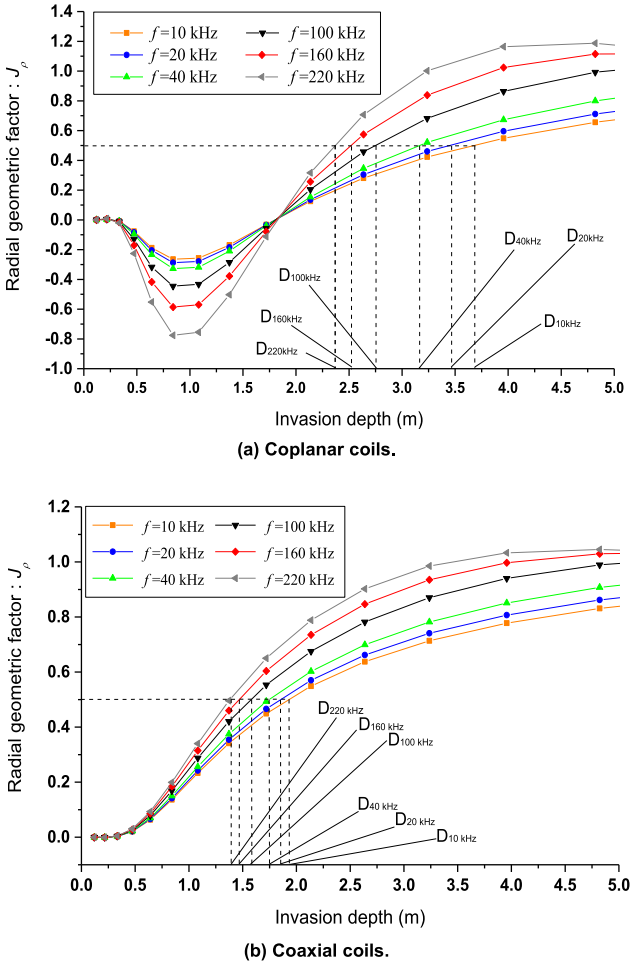

FIGURE 15. Detection depth of coaxial coils and coplanar coils at different frequency.

In addition, we also analyze the D_* with different transmitter-receiver spacing when $f = 20$ kHz, where '$*$' represents the corresponding transmitter-receiver spacing which are set to 38.1 cm (15 in), 53.34 cm (21 in), 68.58 cm (27 in), 99.06 cm (39 in), 137.16 cm (54 in), and 182.88 cm (72 in), respectively, the simulation results are shown in Fig.16. It can be seen from Fig. 16 that the D_* increases with transmitter-receiver spacing, and again, the D_* of coplanar coil is deeper than that of coaxial coil at the same spacing.

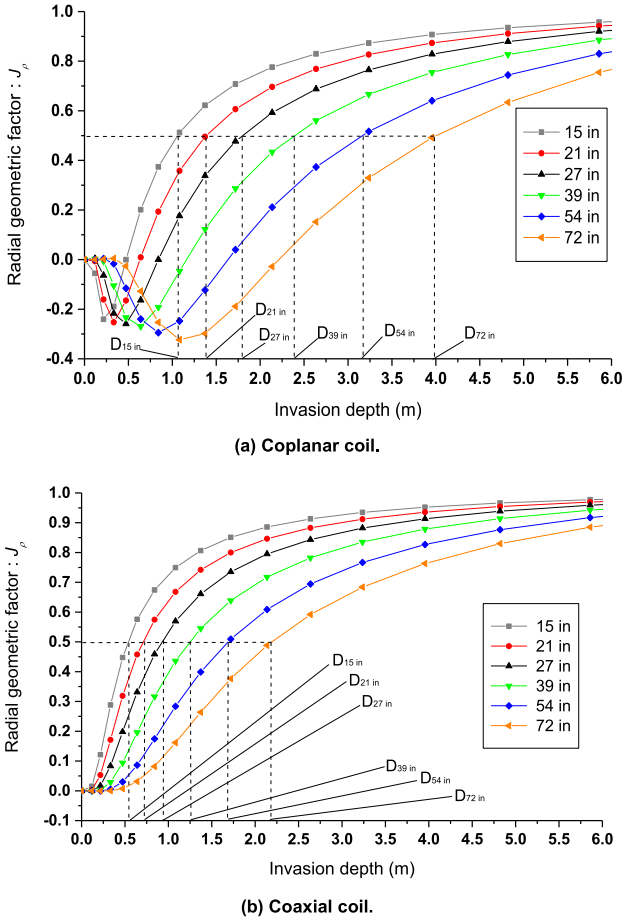

FIGURE 16. Detection depth with different transmitter-receiver spacing when $f = 20$ kHz.

3) PERFORMANCE OF BED RESOLUTION

In order to investigate the bed resolution of MCIL tool, a multi-layer anisotropic formation model with continuous thickness variation is used, the thickness of each layer changes continuously from 3.9 m to 0.28 m. Without loss of generality, the conductivity of each layer is set to $\sigma_h = 2.0$S/m and $\sigma_v = 1.1$ S/m, or $\sigma_h = 1.0$ S/m and $\sigma_v = 0.05$S/m, alternately. The geometry and the apparent conductivity curves are shown in Fig. 17. It can be seen from Fig. 17 that, although the σ_{xx}^a curve is not as regular and

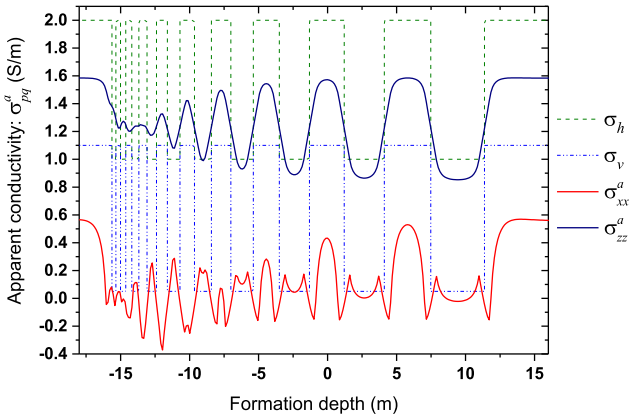

FIGURE 17. Apparent conductivities of multi-layer formation with continuous thickness variation of each layer.

smooth as the σ^a_{zz} curve due to the aforementioned 'horn', it can well reflect the σ_v of the formation, therefore the coplanar coil has better bed resolution than coaxial coil.

V. CONCLUSION

In this article, we analyze the response characteristics of the MCIL tool in anisotropic formation. The PLAMGF method, and the FEM based on a new meshing scheme are presented. The PLAMGF method is derived based on the LMGF [47] and combined with MCIL excitation source and anisotropic formation environment, its effectiveness is verified by numerical experiments, and then it is used to efficiently solve 1-D MCIL problems, including the equivalence of the tool responses in the thin interbed medium and anisotropic medium, as well as the effects of shoulder bed and formation dip on tool responses. According to the EM field distribution and geometry of the solution region, the new meshing scheme based on cylindrical hexahedron element and the flexible mesh meshing strategy is presented, its effectiveness and advantages are verified by numerical experiments, and then it is used for FEM solving the complicated 3-D MCIL problems, including effects of borehole, eccentricity, and invasion on the tool responses, thus effectively reducing the unknown quantities while ensuring the accuracy. Moreover, some key detection performances of coaxial and coplanar coils of MCIL tool are also studied. Numerical experiments demonstrate the validity of our proposed method, and provide the detailed simulation results of the related aspects. The theory and numerical results of this article can provide a useful basis on MCIL modeling, data inversion, construction of the experimental well, and optimal design of the coil system.

APPENDIX

In this appendix, we present the expression of the equivalent transmission line equations which obtained by scalarization of Maxwell's equations and equivalence process of transmission lines. Set the time factor to be $e^{-i\omega t}$, in the case of low frequency, the following Maxwell's equation is satisfied for the field produced by a given magnetic current source $\boldsymbol{M}$ in the formation.

$$\begin{aligned} \nabla \times \boldsymbol{E} &= i\omega u \boldsymbol{H} - \boldsymbol{M} \\ \nabla \times \boldsymbol{H} &= \bar{\boldsymbol{\sigma}} \cdot \boldsymbol{E}, \end{aligned} \tag{A-1}$$

where $\bar{\boldsymbol{\sigma}}$ can be expressed as a diagonal matrix:

$$\bar{\boldsymbol{\sigma}} = \begin{bmatrix} \sigma_{hi} & & \\ & \sigma_{hi} & \\ & & \sigma_{vi} \end{bmatrix}, \quad i = 1, 2, \cdots, N. \tag{A-2}$$

The field in (A-1) is decomposed into transverse (t = x, y) and longitudinal (z) components, and then expressed as the form of transverse Fourier integral,

$$\begin{aligned} \boldsymbol{E} &= \boldsymbol{E}_t + \boldsymbol{E}_z = \int_{-\infty}^{+\infty}\int_{-\infty}^{+\infty} (\tilde{\boldsymbol{E}}_t + \tilde{\boldsymbol{E}}_z) e^{-i\boldsymbol{\kappa}_\rho \cdot \boldsymbol{\rho}} dk_x dk_y \\ \boldsymbol{H} &= \boldsymbol{H}_t + \boldsymbol{H}_z = \int_{-\infty}^{+\infty}\int_{-\infty}^{+\infty} (\tilde{\boldsymbol{H}}_t + \tilde{\boldsymbol{H}}_z) e^{-i\boldsymbol{\kappa}_\rho \cdot \boldsymbol{\rho}} dk_x dk_y, \end{aligned} \tag{A-3}$$

where, $\boldsymbol{\rho} = \hat{\boldsymbol{x}}x + \hat{\boldsymbol{y}}y$ and $\boldsymbol{k}_\rho = \hat{\boldsymbol{x}}k_x + \hat{\boldsymbol{y}}k_y$. By substituting (A-3) into (A-1), we have

$$\begin{aligned} \frac{d}{dz}\tilde{\boldsymbol{E}}_t &= \frac{1}{\sigma_t}(k_t^2 - \lambda^2 \boldsymbol{k}_\rho \boldsymbol{k}_\rho \cdot)(\tilde{\boldsymbol{H}}_t \times \hat{z}) - \tilde{\boldsymbol{M}}_t \times \hat{z} \\ \frac{d}{dz}\tilde{\boldsymbol{H}}_t &= -\frac{1}{i\omega\mu}(k_t^2 - \boldsymbol{k}_\rho \boldsymbol{k}_\rho \cdot)(\hat{z} \times \tilde{\boldsymbol{E}}_t) + \boldsymbol{k}_\rho \frac{\tilde{M}_t}{\omega\mu} \\ \sigma_z \tilde{\boldsymbol{E}}_z &= i\boldsymbol{k}_\rho \cdot (\tilde{\boldsymbol{H}}_t \times \hat{z}) \\ i\omega\mu\tilde{\boldsymbol{H}}_z &= -i\boldsymbol{k}_\rho \cdot (\hat{z} \times \tilde{\boldsymbol{E}}_t) + \tilde{\boldsymbol{M}}_z, \end{aligned} \tag{A-4}$$

where $k_t^2 = i\omega\mu\sigma_t$. Using a set of transverse-coordinate system, then the transverse field can be decomposed into scalar expressions in two directions

$$\begin{aligned} \tilde{\boldsymbol{E}}_t &= \hat{\boldsymbol{u}} V^e + \hat{\boldsymbol{v}} V^h \\ \tilde{\boldsymbol{H}}_t &= -\hat{\boldsymbol{u}} I^e + \hat{\boldsymbol{v}} I^h \\ \tilde{\boldsymbol{M}}_t &= \hat{\boldsymbol{u}} \tilde{M}_u + \hat{\boldsymbol{v}} \tilde{M}_v, \end{aligned} \tag{A-5}$$

where $\hat{\boldsymbol{u}}$ and $\hat{\boldsymbol{v}}$ are the unit vectors of the transverse-coordinate system, in the direction of $\boldsymbol{k}_\rho$ and $\hat{\boldsymbol{z}} \times \boldsymbol{k}_\rho$, respectively.

$$\begin{aligned} \hat{\boldsymbol{u}} &= \hat{\boldsymbol{x}}\frac{k_x}{k_\rho} + \hat{\boldsymbol{y}}\frac{k_y}{k_\rho} \\ \hat{\boldsymbol{v}} &= -\hat{\boldsymbol{x}}\frac{k_y}{k_\rho} + \hat{\boldsymbol{y}}\frac{k_x}{k_\rho}, \end{aligned} \tag{A-6}$$

where $k_\rho = \sqrt{k_x^2 + k_y^2}$. Substituting (A-5) and (A-6) into (A-4), it can be transformed into two independent transmission line equations:

$$\begin{aligned} \frac{dV^p}{dz} &= ik_z^p Z^p I^p + v^p \\ \frac{dI^p}{dz} &= ik_z^p Y^p V^p + i^p, \end{aligned} \tag{A-7}$$

where the upper subscript $p = e$ or h. In this way, the transverse electric field $\tilde{\boldsymbol{E}}_t$ and magnetic field $\tilde{\boldsymbol{H}}_t$ can be

regarded as the voltage and current on the z-direction transmission line. The corresponding propagation wave numbers and characteristic impedances are

$$\begin{aligned} k_z^e &= \sqrt{k_t^2 - \lambda^2 k_\rho^2} \\ k_z^h &= \sqrt{k_t^2 - k_\rho^2} \\ Z^e &= \frac{1}{Y^e} = \frac{k_z^e}{-i\sigma_t} \\ Z^h &= \frac{1}{Y^h} = \frac{\omega\mu}{k_z^h}, \end{aligned} \tag{A-8}$$

where $\lambda^2 = \sigma_t / \sigma_z$. The voltage and current in (A-7) are

$$\begin{aligned} v^e &= -\tilde{M}_v \quad v^h = \tilde{M}_u \\ i^e &= 0 \quad i^h = \frac{k_\rho}{\omega\mu}\tilde{M}_z. \end{aligned} \tag{A-9}$$

It can be seen from (A-4) and (A-5) that electric field and magnetic field can be respectively expressed as

$$\begin{aligned} \tilde{\boldsymbol{E}} &= \hat{\boldsymbol{u}} V^e + \hat{\boldsymbol{v}} V^h + \hat{\boldsymbol{z}} \frac{1}{\sigma_z} i k_\rho I^e \\ \tilde{\boldsymbol{H}} &= -\hat{\boldsymbol{u}} I^h + \hat{\boldsymbol{v}} I^e + \hat{\boldsymbol{z}} \frac{1}{i\omega\mu}(-ik_\rho V^h - \tilde{M}_z). \end{aligned} \tag{A-10}$$

It can be seen from formula (A-10) that the field in the form of spectral domain can be obtained only by solving the transmission voltage and current. If the source in formula (A-7) is a unit source, its solution is just the Green's function of transmission line.

Now let $V_i^p(z, z')$ and $I_i^p(z, z')$ respectively represent the voltage and current generated at z by the unit parallel current source at z', $V_v^p(z, z')$ and $I_v^p(z, z')$ respectively represent the voltage and current generated at z by the unit series voltage source at z', that is, the Green's function of the corresponding transmission line, then the voltage and current generated by arbitrary source can be expressed as

$$\begin{aligned} V^p &= <V_v^p, v^p> + <V_i^p, i^p> \\ I^p &= <I_v^p, v^p> + <I_i^p, i^p>. \end{aligned} \tag{A-11}$$

where <, > represents the inner product of two vectors. According to (A-7) and (A-11), the Green's function of transmission line meets the following equations,

$$\begin{aligned} \frac{dV_i^p(z, z')}{dx} &= ik_z Z^p I_i^p(z, z') \\ \frac{dI_i^p(z, z')}{dx} &= ik_z Y^p V_i^p(z, z') + \delta(z - z') \\ \frac{dV_v^p(z, z')}{dx} &= ik_z Z^p I_v^p(z, z') + \delta(z - z') \\ \frac{dI_v^p(z, z')}{dx} &= ik_z Y^p V_v^p(z, z'). \end{aligned} \tag{A-12}$$

According to the above discussion, the layered medium structure can be equivalent to the transmission line structure with uniform component segments, and the medium parameters of the m$^{\text{th}}$ layer are correspondingly changed into k_{zm}^p and Z_m^p parameters of the m$^{\text{th}}$ section.

REFERENCES

[1] J. H. Moran and K. S. Kunz, "Basic theory of induction logging and application to study of two-coil sondes," *Geophysics*, vol. 27, no. 6, pp. 829–858, Dec. 1962.
[2] S. Chang and B. Anderson, "Simulation of induction logging by the finite-element method," *Geophysics*, vol. 49, no. 11, pp. 1943–1958, Nov. 1984.
[3] W. C. Chew, Z. Nie, Q.-H. Liu, and B. Anderson, "An efficient solution for the response of electrical well logging tools in a complex environment," *IEEE Trans. Geosci. Remote Sens.*, vol. 29, no. 2, pp. 308–313, Mar. 1991.
[4] M. Rabinovich, M. Gonfalini, T. Rocque, B. Corley, D. Georgi, L. Taborovsky, and M. Epov, "Multicomponent induction logging: 10 years after," presented at the 48th Annu. Logging Symp.-Soc. Petrophysicists Well-Log Analysts, Austin, TX, USA, Jun. 2007.
[5] B. Kriegshauser, O. Fanini, S. Forgang, G. Itskovich, M. Rabinovich, L. Tabarovsky, L. Yu, and J. V. D. Horst, "A new multi-component induction logging tool to resolve anisotropic formations," presented at the 40th Annu. Symp., SPWLA, Oslo, Norway, 1999.
[6] M. S. Zhdanov, W. D. Kennedy, and E. Peksen, "Foundation of the tensor induction well logging," *Petrophysics*, vol. 42, no. 6, pp. 588–610, Nov. 2001.
[7] J. Lovell and W. Chew, "Response of a point source in a multicylindrcally layered medium," *IEEE Trans. Geosci. Remote Sens.*, vol. GE-25, no. 6, pp. 850–858, Nov. 1987.
[8] H. Wang, P. So, S. Yang, W. J. R. Hoefer, and H. Du, "Numerical modeling of multicomponent induction well-logging tools in the cylindrically stratified anisotropic media," *IEEE Trans. Geosci. Remote Sens.*, vol. 46, no. 4, pp. 1134–1147, Apr. 2008.
[9] H. Moon, F. L. Teixeira, and B. Donderici, "Stable pseudoanalytical computation of electromagnetic fields from arbitrarily-oriented dipoles in cylindrically stratified media," *J. Comput. Phys.*, vol. 273, pp. 118–142, Sep. 2014.
[10] X. Sun, Z. Nie, A. Li, and X. Lou, "Analysis and correction of borehole effect on the responses of multicomponent induction logging tools," *Progr. Electromagn. Res.*, vol. 85, pp. 211–226, Jan. 2008.
[11] T. Hagiwara, E. J. Banning, R. M. Ostermeier, and S. M. Haugland, "Effects of mandrel, borehole, and invasion for tilt-coil antennas," presented at the SPE 78th Ann. Tech. Conf. Exhib., Denver, CO, USA, Oct. 2003.
[12] D. Hong, J. Xiao, G. Zhang, and S. Yang, "Characteristics of the sum of cross-components of triaxial induction logging tool in layered anisotropic formation," *IEEE Trans. Geosci. Remote Sens.*, vol. 52, no. 6, pp. 3107–3115, Jun. 2014.
[13] D. Hong, W.-F. Huang, and Q. H. Liu, "Radiation of arbitrary magnetic dipoles in a cylindrically layered anisotropic medium for well-logging applications," *IEEE Trans. Geosci. Remote Sens.*, vol. 54, no. 11, pp. 6362–6370, Nov. 2016.
[14] R. H. Hardman and L. C. Shen, "Theory of induction sonde in dipping beds," *Geophysics*, vol. 51, no. 3, pp. 800–809, Mar. 1986.
[15] L. Zhong, J. Li, A. Bhardwaj, L. C. Shen, and R. C. Liu, "Computation of triaxial induction logging tools in layered anisotropic dipping formations," *IEEE Trans. Geosci. Remote Sens.*, vol. 46, no. 4, pp. 1148–1163, Apr. 2008.
[16] S. Yang, D. Hong, W.-F. Huang, and Q. H. Liu, "A stable analytic model for tilted-coil antennas in a concentrically cylindrical multilayered anisotropic medium," *IEEE Geosci. Remote Sens. Lett.*, vol. 14, no. 4, pp. 480–483, Apr. 2017.
[17] W. C. Chew, *Waves and Fields in Inhomogeneous Media*. New York, NY, USA: Van Nostrand, 1990.
[18] H. N. Wang, H. G. Tao, and S. W. Yang, "Study of response of a multicomponent induction logging tool in deviated and layered anisotropic formations by a numerical mode matching algorithm," *Chin. J. Geophys.*, vol. 51, no. 5, pp. 1591–1599, Sep. 2008.
[19] Q. H. Liu, "Electromagnetic field generated by off-axis source in a cylindrically medium with an arbitrary number of horizontal discontinuities," *Geophysics*, vol. 58, no. 5, pp. 616–626, May 1993.
[20] Y. Ren, Y. Chen, M. Meng, Y. Liu, K.-D. Xu, and J. Li, "A surface integral equation formulation for efficient simulation of finite-sized multilayered parallel-plate structure," *IEEE Trans. Microw. Theory Techn.*, vol. 68, no. 7, pp. 2475–2484, Jul. 2020.
[21] D. Wang, Y. Hu, Y. Fang, Q. Zhan, R. Zhang, W.-F. Huang, and Q. H. Liu, "Fast 3-D volume integral equation domain decomposition method for electromagnetic scattering by complex inhomogeneous objects traversing multiple layers," *IEEE Trans. Antennas Propag.*, vol. 68, no. 2, pp. 958–966, Feb. 2020.

[22] Z. Yu, W. Zhang, and Q. H. Liu, "The mixed-order BCGS-FFT method for the scattering of three-dimensional inhomogeneous anisotropic magnetodielectric objects," *IEEE Trans. Antennas Propag.*, vol. 63, no. 12, pp. 5709–5717, Dec. 2015.
[23] Y. Ren, S.-W. Zhao, Y. Chen, D. Hong, and Q. H. Liu, "Simulation of low-frequency scattering from penetrable objects in layered medium by current and charge integral equations," *IEEE Trans. Geosci. Remote Sens.*, vol. 56, no. 11, pp. 6537–6546, Nov. 2018.
[24] Y. P. Chen, W. C. Chew, and L. Jiang, "A new Green's function formulation for modeling homogeneous objects in layered medium," *IEEE Trans. Antennas Propag.*, vol. 60, no. 10, pp. 4766–4776, Oct. 2012.
[25] Y. Ren, S.-W. Zhao, H. Hu, and Y. Chen, "Hydraulic fracture scattering simulation by thin dielectric structure-based higher order surface integral equations," *IEEE Trans. Geosci. Remote Sens.*, vol. 58, no. 3, pp. 1803–1811, Mar. 2020.
[26] Z. Wu, Y. Fan, J. Wang, R. Zhang, and Q. H. Liu, "Application of 2.5-D finite difference method in logging-while-drilling electromagnetic measurements for complex scenarios," *IEEE Geosci. Remote Sens. Lett.*, vol. 17, no. 4, pp. 577–581, Apr. 2020.
[27] M. S. Novo, L. C. da Silva, and F. L. Teixeira, "Three-dimensional finite-volume analysis of directional resistivity logging sensors," *IEEE Trans. Geosci. Remote Sens.*, vol. 48, no. 3, pp. 1151–1158, Mar. 2010.
[28] D. Pardo, L. Demkowicz, C. Torres-Verdín, and C. Michler, "PML enhanced with a self-adaptive goal-oriented *hp*-finite element method: Simulation of through-casing borehole resistivity measurements," *SIAM J. Sci. Comput.*, vol. 30, no. 6, pp. 2948–2964, Jan. 2008.
[29] M. M. Ilic and B. M. Notaros, "Higher order hierarchical curved hexahedral vector finite elements for electromagnetic modeling," *IEEE Trans. Microw. Theory Techn.*, vol. 51, no. 3, pp. 1026–1033, Mar. 2003.
[30] Q. Sun, Q. Ren, Q. Zhan, and Q. H. Liu, "3-D domain decomposition based hybrid finite-difference time-domain/finite-element time-domain method with nonconformal meshes," *IEEE Trans. Microw. Theory Techn.*, vol. 65, no. 10, pp. 3682–3688, Oct. 2017.
[31] J. Ma, J.-M. Jin, and Z. Nie, "A nonconformal tree-cotree splitting and improved transmission condition subsurface detection problems," *IEEE Trans. Geosci. Remote Sens.*, vol. 52, no. 1, pp. 355–364, Jan. 2014.
[32] J. Shen, "Modeling 3-D electromagnetic responses of the magnetic dipole in frequency domain by using the edge finite element method," *Chin. J. Geophys.*, vol. 19, no. 6, pp. 537–543, 2002.
[33] M. E. Everett, E. A. Badea, L. C. Shen, G. A. Merchant, and C. J. Weiss, "3-D finite element analysis of induction logging in a dipping formation mark," *IEEE Trans. Geosci. Remote Sens.*, vol. 39, no. 7, pp. 2244–2252, 2001.
[34] M. G. Persova, Y. G. Soloveichik, P. A. Domnikov, and D. Vagin, "Finite element modeling of three-dimensional geoelectromagnetic field excited by arbitrarily oriented induction source," in *Proc. 12th Int. Conf. Actual Problems Electron. Instrum. Eng.*, 2014, pp. 598–602.
[35] Z. Chimendsurong and H. Wang, "Forward modeling of induction well logging tools in dipping boreholes and their response," *Chin. J. Comput. Phys.*, vol. 20, no. 2, pp. 161–168, Mar. 2003.
[36] J. Xiao and G. Zhang, "Computation of induction logging response in horizontal and highly-deviated wells," *Chin. J. Geophys.*, vol. 38, no. 3, pp. 403–496, May 1995.
[37] G. Xing and F. L. Teixeira, "An efficient rescaled formulation for tensor Green's function computation in cylindrical multilayered media," *IEEE Trans. Antennas Propag.*, vol. 63, no. 12, pp. 5677–5685, Dec. 2015.
[38] G. Xing, X. Zhang, and F. L. Teixeira, "Computation of tensor Green's functions in uniaxial planar-stratified media with a rescaled equivalent boundary approach," *IEEE Trans. Antennas Propag.*, vol. 66, no. 4, pp. 1863–1873, Apr. 2018.
[39] Q. Sun, R. Zhang, Q. Zhan, and Q. H. Liu, "Multiscale hydraulic fracture modeling with discontinuous Galerkin frequency-domain method and impedance transition boundary condition," *IEEE Trans. Geosci. Remote Sens.*, vol. 55, no. 11, pp. 6566–6573, Nov. 2017.
[40] M. Luo, Y. Lin, and Q. H. Liu, "Spectral methods and domain decomposition for nanophotonic applications," *Proc. IEEE*, vol. 101, no. 2, pp. 473–483, Feb. 2013.
[41] Y. Zhou, L. Shi, N. Liu, C. Zhu, H. Liu, and Q. H. Liu, "Spectral element method and domain decomposition for low-frequency subsurface EM simulation," *IEEE Geosci. Remote Sens. Lett.*, vol. 13, no. 4, pp. 550–554, Apr. 2016.
[42] J. Ma, J.-M. Jin, and Z. Nie, "A nonconformal FEM-DDM with tree-cotree splitting and improved transmission condition for modeling subsurface detection problems," *IEEE Trans. Geosci. Remote Sens.*, vol. 52, no. 1, pp. 355–364, Jan. 2014.
[43] R. Zhang, Z. Wu, Q. Sun, M. Zhuang, Q.-M. Cai, D. Wang, and Q. H. Liu, "Memory-efficient 3-D LWD solver with the flipped total field/scattered field-based DGFD method," *IEEE Geosci. Remote Sens. Lett.*, early access, Nov. 12, 2020, doi: 10.1109/LGRS.2019.2950659.
[44] Z.-G. Wu, S.-G. Deng, X.-Q. He, R. Zhang, Y.-R. Fan, X.-Y. Yuan, Y.-Z. Wu, and Q. H. Liu, "Numerical simulation and dimension reduction analysis of electromagnetic logging while drilling of horizontal wells in complex structures," *Petroleum Sci.*, vol. 17, no. 3, pp. 645–657, Apr. 2020.
[45] X. Sun and Z. Nie, "Application of higher order hierarchical vector finite element method in multicomponent electromagnetic induction problem," in *Proc. Antennas Propag. Conf.*, Loughborough, U.K., vol. 91, Apr. 2008, pp. 413–416.
[46] L. B. Felsen and N. Marcuvitz, *Radiation and Scattering of Waves*. Englewood Cliffs, NJ, USA: Prentice-Hall, 1973.
[47] K. A. Michalski and J. R. Mosig, "Multilayered media Green's functions in integral equation formulations," *IEEE Trans. Antennas Propag.*, vol. 45, no. 3, pp. 508–519, Mar. 1997.
[48] H. Wang, S. Yang, and M. Chang, "Fast modeling of lateral resistivity logging in horizontal anisotropic layers and its application," *Well Logging Techn.*, vol. 22, no. 1, pp. 28–31, Jan. 1998.
[49] A. Q. Howard and W. C. Chew, "Electromagnetic borehole fields in a layered dipping bed environment with invasion," *Geophysics*, vol. 57, no. 3, pp. 451–465, Mar. 1992.
[50] D. Li, D. R. Wilton, D. R. Jackson, J. Chen, and H. Wang, "Efficient computation of Green's functions for lossy uniaxial anisotropic layered media," *Radio Sci.*, vol. 54, no. 3, pp. 196–214, Mar. 2019.
[51] Y. A. Tuchkin, A. Sanli, and F. Dikmen, "Efficient computation of Green's function for 1-D periodic structures," *IEEE Antennas Wireless Propag. Lett.*, vol. 19, no. 3, pp. 373–377, Mar. 2020.
[52] G. Chen, H. Wang, J. Yao, Z. Han, and S. Yang, "An efficient algorithm of the electromagnetic dyadic Green's function in a horizontal-layered anisotropic medium," (in Chinese), *Acta. Phys. Sinica*, vol. 58, no. 3, pp. 1068–1618, Mar. 2009.
[53] P. R. Atkins and W. C. Chew, "Fast computation of the dyadic Green's function for layered media via interpolation," *IEEE Antennas Wireless Propag. Lett.*, vol. 9, pp. 493–496, 2010.
[54] Y. P. Chen, W. C. Chew, and L. Jiang, "A novel implementation of discrete complex image method for layered medium Green's function," *IEEE Antennas Wireless Propag. Lett.*, vol. 10, pp. 419–422, May 2011.
[55] K. A. Michalski, "Extrapolation methods for sommerfeld integral tails," *IEEE Trans. Antennas Propag.*, vol. 46, no. 10, pp. 1405–1418, Oct. 1998.
[56] C. R. Berg, "A simple, effective-medium model for water saturation in porous rocks," *Geophysics*, vol. 60, no. 4, pp. 1070–1080, Jul. 1995.
[57] J. M. V. A. Koelman and A. de Kuijper, "An effective medium model for the electric conductivity of an N-component anisotropic and percolating mixture," *Phys. A, Stat. Mech. Appl.*, vol. 247, nos. 1–4, pp. 10–22, Dec. 1997.
[58] Y. Bao and J. Song, "Modeling of multilayered anisotropic media using effective medium theory," in *Proc. IEEE Int. Symp. Antennas Propag. USNC/URSI Nat. Radio Sci. Meeting*, Jul. 2016, pp. 2097–2098.
[59] R. Zhang, Q. Sun, Z. Wu, Y. Fang, Y. Hu, W.-F. Huang, Y. Mao, and Q. H. Liu, "Fast induction logging modeling with hierarchical sudoku meshes based on DGFD," *IEEE Geosci. Remote Sens. Lett.*, vol. 16, no. 11, pp. 1683–1687, Nov. 2019.
[60] Q. Zhan, M. Zhuang, Q. Sun, Q. Ren, Y. Ren, Y. Mao, and Q. H. Liu, "Efficient ordinary differential equation-based discontinuous Galerkin method for viscoelastic wave modeling," *IEEE Trans. Geosci. Remote Sens.*, vol. 55, no. 10, pp. 5577–5584, Oct. 2017.
[61] J. M. Jin, *The Finite Element Method in Electromagnetics*, 2nd ed. Hoboken, NJ, USA: Wiley, 2002.
[62] Y. P. Chen, L. Jiang, S. Sun, W. C. Chew, and J. Hu, "Calderón preconditioned PMCHWT equations for analyzing penetrable objects in layered medium," *IEEE Trans. Antennas Propag.*, vol. 62, no. 11, pp. 5619–5627, Nov. 2014.
[63] X. Y. Sun and Z.-P. Nie, "Vector finite element analysis of multicomponent induction response in anisotropic formations," *Prog. Electromagn. Res.*, vol. 81, pp. 21–39, Jan. 2008.

[64] B. Després, P. Joly, and J. E. Roberts, "A domain decomposition method for the harmonic Maxwell equation," in *Iterative Methods Linear Algebra*. Amsterdam, The Netherlands: North Holland, 1992, pp. 475–484.
[65] J.-D. Benamou and B. Desprès, "A domain decomposition method for the Helmholtz equation and related optimal control problems," *J. Comput. Phys.*, vol. 136, no. 1, pp. 68–82, Sep. 1997.
[66] S.-C. Lee, M. N. Vouvakis, and J.-F. Lee, "A non-overlapping domain decomposition method with non-matching grids for modeling large finite antenna arrays," *J. Comput. Phys.*, vol. 203, no. 1, pp. 1–21, Feb. 2005.
[67] J. S. Shen, "Modeling of the 3-D electromagnetic responses to the anisotropic medium by the edge finite element method," *Well Logging Technol. China*, vol. 28, pp. 11–15, Feb. 2004.
[68] L. R. Lovell and W. C. Chew, "Effect of tool eccentricity on some electrical well-logging tools," *IEEE Trans. Geosci. Remote Sens.*, vol. 28, no. 1, pp. 127–136, Jan. 1990, doi: 10.1109/36.45750.
[69] G. Zhou, H. Pan, and H. Han, "The calculation and analysis of array induction logging HRAI instrument's response," in *Proc. 8th Int. Conf. Fuzzy Syst. Knowl. Discovery (FSKD)*, Shanghai, China, 2011, pp. 2570–2574, doi: 10.1109/FSKD.2011.6019973.
[70] H. Ma, "Research and application on the theory and method of AIL array induction logging," Ph.D. dissertation, Inst. Geophys. Geomat., China Univ. Geosci., Beijing, China, 2007.
[71] Z. Tian, Y. Sun, G. Liu, *Induction Logging Theory and Its Application*. Beijing, China: Petroleum Industry Press, 1984.

YUEHUI LI received the M.S. and Ph.D. degrees from the University of Electronic Science and Technology of China, in 2004 and 2011, respectively. She is currently an Associate Professor with the School of Computer and Software Engineering, Xihua University, Chengdu, China. Her current research interests include computational electromagnetics, computer simulation, and numerical technology. She is a member of the ACM.

XIANGYANG SUN received the Ph.D. degree in electromagnetics and microwave technology from the University of Electronic Science and Technology of China, Chengdu, China, in 2008. He is currently an Associate Professor with the School of Electronic Science and Engineering, University of Electronic Science and Technology of China. His current research interests include electromagnetics in inhomogeneous medium and the application of electromagnetics in geophysics.

GUODONG SU received the B.S. degree from Quanzhou Normal University, in 2011. His research interests include computational electromagnetics and computer technology.

MIN WANG received the M.S. degree in economics and the M.S. degree in computer engineering and automation from Örebro University, in 2009 and 2011, respectively. She is currently a Lecturer with the School of Computer and Software Engineering, Xihua University, Chengdu, China. Her current research interests include computational electromagnetics, electromagnetic detection systems, and machine learning. She is a member of the ACM.

RUI LI received the B.S. degree from Xihua University, Chengdu, China, in 2011, where he is currently pursuing the M.S. degree with the School of Computer and Software Engineering. His research interests include computational electromagnetics and machine learning.